Supporting Information

Coiled Conformation Hollow Carbon Nanosphere Cathode and Anode for High-Energy Density and Ultrafast Chargeable Hybrid Energy Storage

Gi Hwan Kim[1], Won Ho Choi[1], Jae Won Choi[1], Keon-Han Kim[1,2], Dong Gyu Park[1], Min Gyu Park[1], Min Gyu Kim[3], Haeseong Jang[3], Un-Hyuck Kim[4] and Jeung Ku Kang[1,*]

[1]*Department of Materials Science and Engineering, Korea Advanced Institute of Science and Technology (KAIST), 291 Daehak-ro, Yuseong-gu, Daejeon 34141, Republic of Korea*

[2] *Department of Chemistry, University of Oxford, 12 Mansfield Rd., Oxford OX1 3TA, United Kingdom*

[3]*Beamline Research Division, Pohang Accelerator Laboratory, 77 Cheongam-ro, Nam-gu, Pohang 37673, Republic of Korea*

[4]*Department of Energy Engineering, Hanyang University, 222 Wangsimni-ro, Seongdong-gu, Seoul 04763, Republic of Korea*

**E-mail: jeungku@kaist.ac.kr*

Supporting Information Contents

-Section S1. Method details

-Section S2. Structural characterizations details

-Section S3. Fabrication and electrochemical characterizations of half and full cells details

-Section S4. Supporting figures and tables

Figure S1. FT-IR spectra of B:B RS and Q:B RS

Figure S2. HR-TEM images of B:B RS and Q:B RS

Figure S3. HR-TEM images of B:B HC and Q:B HC

Figure S4. TGA data of B:B HC and Q:B HC under air condition

Figure S5. Diameters of silica nanospheres controlled conditions

Figure S6. TEM images of B:B RS and Q:B RS before carbonization and silica core etching processes

Figure S7. TEM images of hollow carbons (HCs) synthesized using the different ratios of resorcinol and melamine

Figure S8. XPS survey spectra of B:B HC and Q:B HC

Figure S9. Raman spectroscopy data of B:B HC and Q:B HC

Figure S10. Nitrogen adsorption/desorption isotherms curve and pore distribution of HCs

Figure S11. Nitrogen adsorption/desorption isotherm curves and specific surface area of same resorcinol amount derived HC with or without melamine addition

Figure S12. Nitrogen adsorption/desorption isotherms curve and pore distribution of B:B RS and Q:B RS

Figure S13. TGA data of B:B RS and Q:B RS during the carbonization process under Ar atmosphere

Figure S14. HADDF-STEM images of Mono Ge-Q:B HC

Figure S15. HADDF-STEM images of Ge-Q:B HC derived from the intermediate Ge precursor concentration

Figure S16. HADDF-STEM images of Bulk Ge-Q:B HC having the aggregated bulk Ge particles

Figure S17. TEM and EDS mapping images. of Bulk Ge-Q:B HC

Figure S18. XRD patterns of Mono Ge-Q:B HC and Bulk Ge-Q:B HC

Figure S19. TEM images of Mono Ge-Q:B RS and Bulk Ge-Q:B RS structures

Figure S20. TGA analysis in air atmosphere condition of Mono Ge-Q:B HC

Figure S21. XPS Ge 3d spectra of Mono Ge-Q:B HC

Figure S22. XANES and EXAFS of Ge-Q:B HC with the different Ge precursor concentrations

Figure S23. CV curves of B:B HC and Q:B HC

Figure S24. CV curves of samples derived from the different melamine contents

Figure S25. Specific capacities of HC samples derived from the different melamine contents

Figure S26. Specific capacities comparison of Q:B HC and YP-80F commercial activated carbon

Figure S27. Energy storage contribution ratios of Q:B HC cathode

Figure S28. Nyquist plots of Q:B HC and B:B HC under the open circuit voltage(OCV) state condition

Figure S29. Cycling stability over 10,000 cycles and coulombic efficiency of Q:B HC

Figure S30. TEM images of a Q:B HC electrode after 1,000 charging-discharging cycles

Figure S31. Specific capacities of Mono Ge-Q:B HC and Q:B HC from the GCD curves

Figure S32. Comparison of gravimetric capacities and volumetric capacities of Mono Ge-Q:B HC

Figure S33. CV curves of Mono Ge-Q:B HC with the different scan rates

Figure S34. Energy storage contribution ratios of Mono Ge-Q:B HC

Figure S35. GCD profiles of Mono Ge-Q:B HC

Figure S36. GITT curves and lithium-ion diffusion coefficients

Figure S37 Nyquist plots of Ge powder, Bulk Ge-Q:B HC, and Mono Ge-Q:B HC in the OCV state condition

Figure S38. Cycling performance of the of Mono Ge-Q:B HC, Bulk Ge-Q:B HC and Ge powder

Figure S39. TEM images of Ge-Q:B HC samples after 50 charging/discharging cycles

Figure S40. CV curves of Ge-Q:B HC//Q:B HC full cell with different electrode mass ratio of Ge–Q:B HC to Q:B HC

Figure S41. Capacity retention curves of Ge-Q:B HC//Q:B HC and Ge powder//Q:B HC full cell

Figure S42. Ragone plots of Ge-Q:B HC//Q:B HC full cells on the different mass loadings

Figure S43. Photos and ragone plots of fabricated Ge-Q:B HC//Q:B HC pouch-type full cells

Figure S44. GCD profiles of the three-electrode full cell as well as the potential range of each electrode

Table S1. Electrochemical performances of Ge-Q:B HC//Q:B HC hybrid energy storage full cells at the different current densities

Table S2. Electrochemical performances of previous works on non-aqueous HES full cells and this work

Table S3. Electrochemical performances of previous works on aqueous HES full cells and dual carbon electrode capacitors as well as this work

-Section S5. References

Section S1. Methods details

S1.1. Synthesis of silica nanospheres

Silica nanospheres were obtained by the hydrolysis of tetraethylorthosilicate (TEOS) in an ethanol solvent containing DI water under the base condition using ammonia solution via Stöber method. TEOS (3.46 mL, 12 mmol) was dropwise added to the solution containing 10ml of DI water, some amounts of ethanol and 3ml of ammonia water (25 wt. %) under the stirring condition (200 rpm) at room temperature for 2 h. Silica nanosphere products were separated by centrifugation (10000 rpm, 10 min) and washed with deionized water three times. The obtained solid product was dried at 80 °C for 24 h.

S1.2. Synthesis of quinoid:benzenoid (Q:B) unit resin-based hollow carbon (Q:B HC) and B:B HC nanospheres

Silica core-quinoid:benzenoid resin shell (Q:B-RS) structures were synthesized by a polymer coating process. 0.5 g of the obtained silica nanospheres and 100 mL of DI water were added into a 125 mL round-bottom flask. Then, 0.088g (0.8mmol) of resorcinol, 0.152g (1.2mmol) of melamine, 1.2 g of cetyltrimethylammonium bromide (CTAB), 35 mL ethanol, and 1 mL of ammonia water were added in the silica solution continuously. After 30 min, 0.42 ml of formaldehyde solution was dropwise added to the mixed solution and the solution is heated at 70 °C with stirring for 5 min and stirring 24 h more under room temperature. Then, Q:B RS products were separated by centrifugation (10000 rpm, 10 min), washed with ethanol and DI water, and dried at 60 °C for 24 h. Q:B HC nanospheres were obtained after carbonization at 800 °C for 2 h in the 5 °C/min heating rate under the Ar atmosphere in a tube furnace. Next, silica nanospheres were etched by hydrofluoric acid solution (HF, 5 wt. %) for 4 h. . Q:B and B:B HC nanospheres were prepared in the same conditions and procedures with the same moles of resorcinol and melamine. Meanwhile, B:B HC was synthesized using only resorcinol without melamine addition. Hence, Q:B HC and B:B HC nanospheres were prepared using different melamine contents.

S1.3. Synthesis of Ge-embedded HC (Ge-Q:B HC) nanospheres

Silica core-mono nuclear GeO_x embedded HC nanospheres were synthesized using the similar procedures to the synthesis of Q:B HC nanospheres. 0.132g (1.2mmol) of resorcinol and 0.46ml germanium tetrachloride were dissolved in 50ml anhydrous ethanol with sonication to form a homogeneous precursor solution. 0.5 g of the obtained silica nanospheres and 100 mL of DI water were added into a 125 mL round-

bottom flask, in which silica nanospheres were dispersed by sonication. Then, 0.083 g (0.8 mmol) of melamine, 1.2 g of CTAB, and 5 mL of ammonia water were added in the silica solution and stirred continuously. After 30 min, 0.42 ml of formaldehyde solution was dropwise added to the mixed solution and heated at 70 °C with stirring. Next, the ethanol precursor solution was dropwise added to the mixed solution and kept for 5 min. Afterward, the solution was stirred 24 h more under room temperature.Then, the products was separated by centrifugation (10000 rpm, 10 min), washed with ethanol and DI water, and then dried at 60 °C for 24 h. Ge-Q:B HC nanospheres were obtained after carbonization and reduction step at 800 °C for 2 h with the 5 °C/min heating rate under the steady-state Ar and H_2 atmosphere in a tube furnace. Next, silica nanospheres were etched by HF acid solution (5 wt. %) for 4 h. Ge-Q:B HC nanospheres with different germanium contents were prepared using different germanium chloride amounts.

Section S2. Structural characterizations details

The transmission electron microscopy (TEM) and high resolution TEM (HR-TEM) images were taken from the Tecnai G2 F30 S-Twin (FEI) and JEM-ARM-200F Cs-corrected TEM (JEOL). Moreover, the energy dispersive spectrometer (EDS) attached to the TEM was used to obtain the elemental mapping in the scanning TEM (STEM) mode. The Fourier transform-infrared (FT-IR) spectra were collected from the KBr pellet method using the FT-TR-6100 (JASCO). The CP/MAS/^{13}C-NMR data were obtained by the solid NMR 600 MHz (Varian) with 3.2 nm NB triple resonance MAS solids probe. The X-ray photoelectron spectroscopy (XPS) spectra were collected using a Thermo VG Scientific K-alpha spectrometer (Thermo Scientific, USA) using Al-Kα radiation at 350 W (3 mA). The powder X-ray diffraction (PXRD) patterns were measured with a Smartlab diffractometer (Rigaku, Japan) using a Cu kα operating condition of 40 kV and 30 mA. The X-ray absorption near edge structure (XANES) and extended X-ray absorption fine structure (EXAFS) measurements were conducted in 10C beamline at the Pohang Accelerator Laboratory (PAL). The near edge X-ray absorption fine structure (NEXAFS) measurements were conducted in 4D beamline at PAL. The thermal gravimetric analysis (TGA) was performed by TG-209 (Netzsch) in nitrogen atmosphere and air atmosphere. The Raman spectra were obtained by an ARAMIS dispersive-Raman(Horiba) with 514nm of Ar-ion laser. Moreover, the surface area and pore distribution were obtained from the N_2 adsorption/desorption isotherm performed on a Quadrasorb automatic volumetric instrument. The liquid nitrogen bath (77 K), ultra-high purity grade nitrogen, and helium were used for experiments and the samples were pretreated by the evacuating process at 100 °C for 24 h. Next, the sample was filled with the

helium gas. The Brunaner–Emmett–Teller (BET) surface area was determined using the adsorption branches of N_2 isotherms. The pore distribution and pore volume were analyzes using the quenched solid density functional theory (QSDFT) and the t-plot method, respectively.

Section S3. Fabrication and electrochemical characterizations of half and full cells details

S3.1. Fabrication of half-cell and full-cell devices

The slurry for a cathode was prepared by mixing 56mg of Q:B HC (80 wt.%), 7mg of carbon black (Super C65, 10 wt.%), and 7mg of poly (vinylidene fluoride) binder (PVDF, 10 wt.%) in 2ml of N-methyl-2-pyrrolidone (NMP). The slurry was then pasted on a pure Al foil with 40 μm thickness using a doctor blade and dried in a vacuum oven at 80 °C overnight. The 2.95mg of working electrode on Al foil was assembled into CR2032-type cell in an argon-filled glove box with a pure lithium metal (Honjo Chemical Co.) as the counter/reference electrode. 0.1ml of 1M lithium hexafluorophosphate ($LiPF_6$) was dissolved in a mixture of ethylene carbonate (EC)/diethyl carbonate (DEC) (v:v = 1/1) as the electrolyte, monolayer polypropylene membrane (Celgard 2400) was used as the separator. Moreover, the slurry for an anode was prepared by mixing 49mg of Ge-Q:B HC (70 wt.%), 14mg of carbon black (Super C65, 20 wt.%), and 7mg of poly (vinylidene fluoride) binder (PVDF, 10 wt.%) in 2ml of NMP to make a slurry. The slurry was then pasted on a pure Cu foil with 40 μm thicknesses using a doctor blade and dried in a vacuum oven at 80 °C overnight. The 3.54mg of working electrode on Cu foil was assembled into using a CR2032-type cell in an argon-filled glove box with a pure lithium metal (Honjo Chemical Co.) as the counter/reference electrode. 0.1ml of 1 M $LiPF_6$ dissolved in a mixture of EC/DEC (v:v = 1/1) as the electrolyte, and monolayer polypropylene membrane (Celgard 2400) was used as the separator. Furthermore, Ge-Q:B HC anode with Q:B HC cathode were into a coin-type full cell. Before cell fabrication, Ge-Q:B HC anode was pre-lithiated to prevent the loss of Li ions during operation. In the same method as the half cell, the Ge-Q:B HC working electrode was assembled into using a CR2032-type cell in an argon-filled glove box with a pure lithium metal (Honjo Chemical Co.), 0.1ml of 1 M $LiPF_6$ in EC/DEC (v:v = 1/1) as the electrolyte, and monolayer polypropylene membrane (Celgard 2400) as the separator. The assembled cells were charged up to 0.01V (vs. Li/Li^+) for the pre-lithiation process. After charging, the charged cell is disassembled and extracted the pre-lithiated Ge-Q:B HC electrode is used as the anode of the full cell. The full cell is fabricated with the mass ratio of Ge-Q:B HC anode to Q:B HC cathode was 1:3.4 for charge balance in a full cell device with various total mass (3.98mg, 5.24mg, 10.51mg). The 0.1ml of 1 M $LiPF_6$ in EC/DEC (v:v = 1/1) with 5 wt.% fluoroethylene

carbonate (FEC) was used as the electrolyte, and monolayer polypropylene membrane (Celgard 2400) was used as the separator in full cell. The pouch-type cells wrapped in Al were fabricated using the same compositions as that used in the coin-type cells. The pouch-type cells were assembled with the size of 3 cm × 5 cm anode and cathode electrodes and contained 0.8 mL electrolyte. Each layer between the electrodes was wrapped with a separator. The electrode mass loadings of Ge-Q:B HC on the Cu foil and Q:B HC on Al foil were 8.58 mg and 28.41 mg, respectively.

S3.2. Electrochemical characterizations

Q:B HC cathode was evaluated in the potential range of 2 V to 4.5 V (vs. Li/Li^+) at room temperature using a potentiostat (Bio-logic,VSP). The Ge-Q:B HC anode was evaluated in the potential range of 0.01 V to 3 V (vs. Li/Li^+) at room temperature using a battery cycler (Wonatech, WBCS-3000). In addition, the electrochemical impedance spectroscopy (EIS) measurement was conducted using a potentiostat (Bio-logic, VSP) on the open circuit voltage. The diffusion coefficient was determined from the GITT data using the following equation of

$$D_{Li^+} = \frac{4}{\pi\tau}\left(\frac{V_m n_m}{S}\right)^2 \left(\frac{\Delta E_s}{\Delta E_t}\right)^2 \qquad \text{S1}$$

where τ, V_m, n_m, and S refers to the time of the current pulse, the molar volume of the electrode, the number of moles, and the electrode/electrolyte contact area, respectively. ΔE_s and ΔE_t are defined as the steady-state potential change and the potential change due to the charging pulse, respectively. The cell-discharge capacity was calculated using the following relationship of

$$C = i \times \frac{t}{m\Delta V} \qquad \text{S2}$$

where i is the applied current (A), t is the discharge time (s), m is the total weight (g) of active materials in two electrodes, and ΔV is the potential difference (V). Besides, power density (P, W kg^{-1}) and energy density (E, Wh kg^{-1}) were calculated using the following equations of

$$P = V \times \frac{i}{m} \qquad \text{S3}$$

$$E = P \times \frac{t}{3600} \qquad \text{S4}$$

$$V = (V_{\max} + V_{\min}) \times \frac{1}{2} \qquad \text{S5}$$

in which i is the applied current, V is the voltage of cell time, t is the discharge time, and m is the weight of total electrodes, respectively. Moreover, to analyze the operation potential of each electrode for a full cell, the cell was assembled with Ge-Q:B HC anode, Q:B HC cathode, and lithium metal foil as the reference

electrode in a three-electrode configuration (Wellcos, HS-3E TK). The full cell was operated in the voltage range of 0.01 V to 4.5V at room temperature using a potentiostat (Bio-logic, VSP).

S3.3. Ultrafast charging module analysis

An ultrafast charging module consists of the hybrid capacitor full cell part, the photovoltaic solar cell part for charging, and the mini-motor operating part with the windmill model. Three fabricated Ge-Q:B HC//Q:B HC hybrid energy storage full cells are connected and charged by the solar cell when the light is irradiated. The mini-motor operates only when switched on. The solar cell demonstrates the 5V maximum voltage and 65 mA maximum current operation through the 100 mW cm^{-2} AM 1.5G of Xenon lamp.

Section S4. Supporting figures and tables

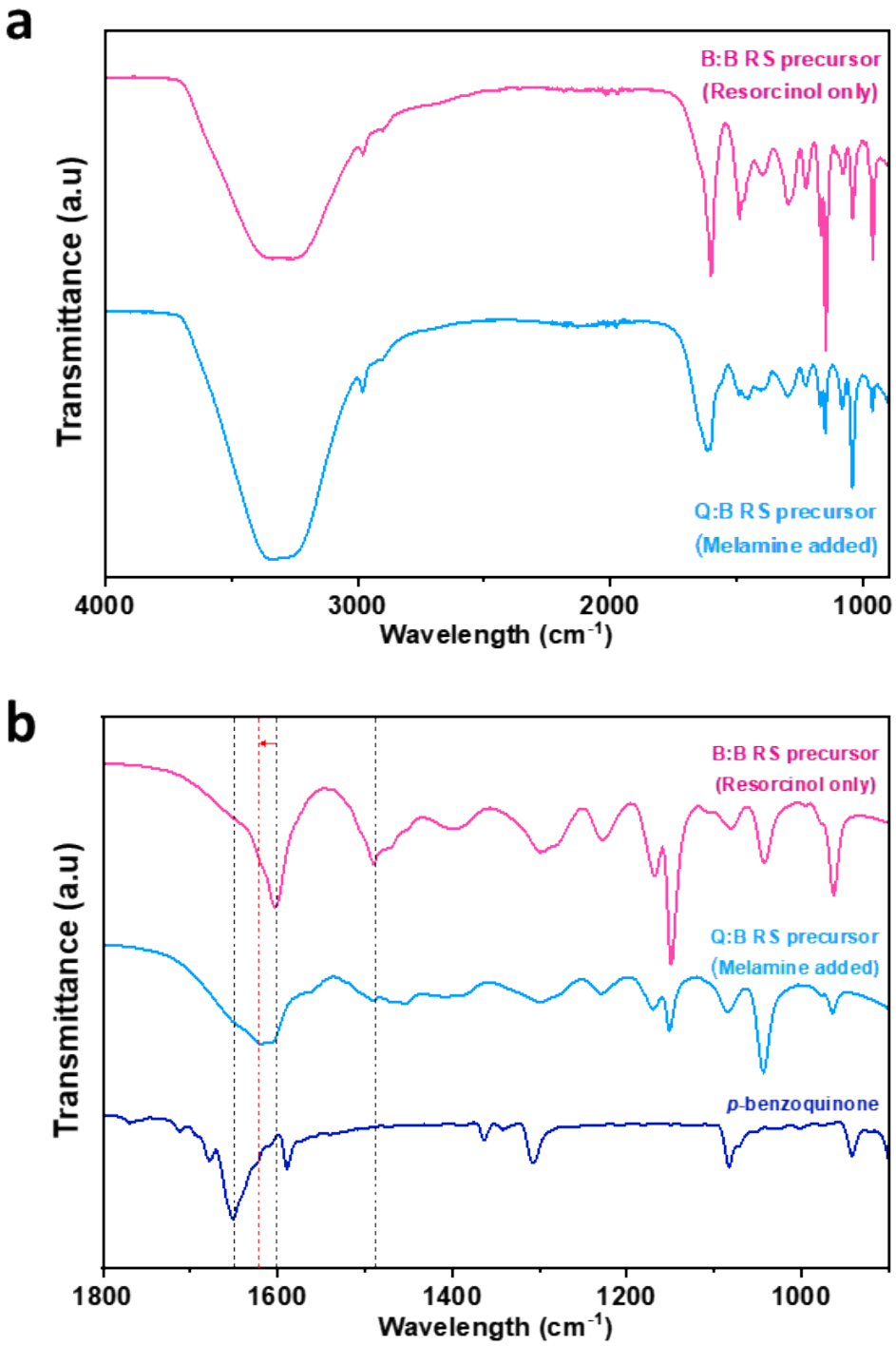

Figure S1 | FT-IR spectra. Those for (**a**) B:B RS and Q:B RS precursors, and (**b**) B:B RS precursor, Q:B RS precursor, and *p*-benzoquinone in the enlarged short wavelength range.

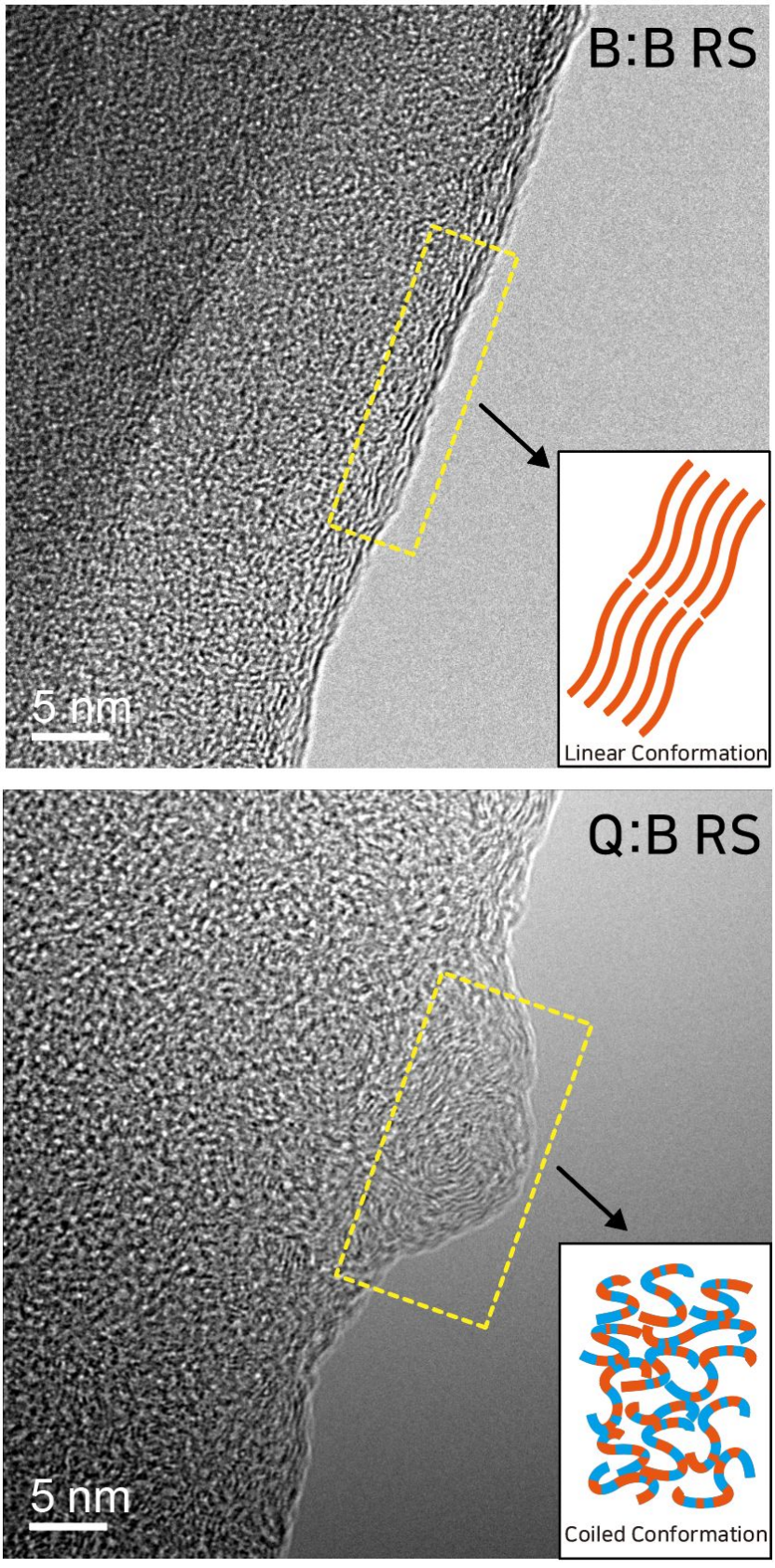
B:B RS
5 nm
Linear Conformation
Q:B RS
5 nm
Coiled Conformation

Figure S2 | HR-TEM images. Those for B:B RS with stacked linear conformation polymer and Q:B RS with coiled conformation polymer.

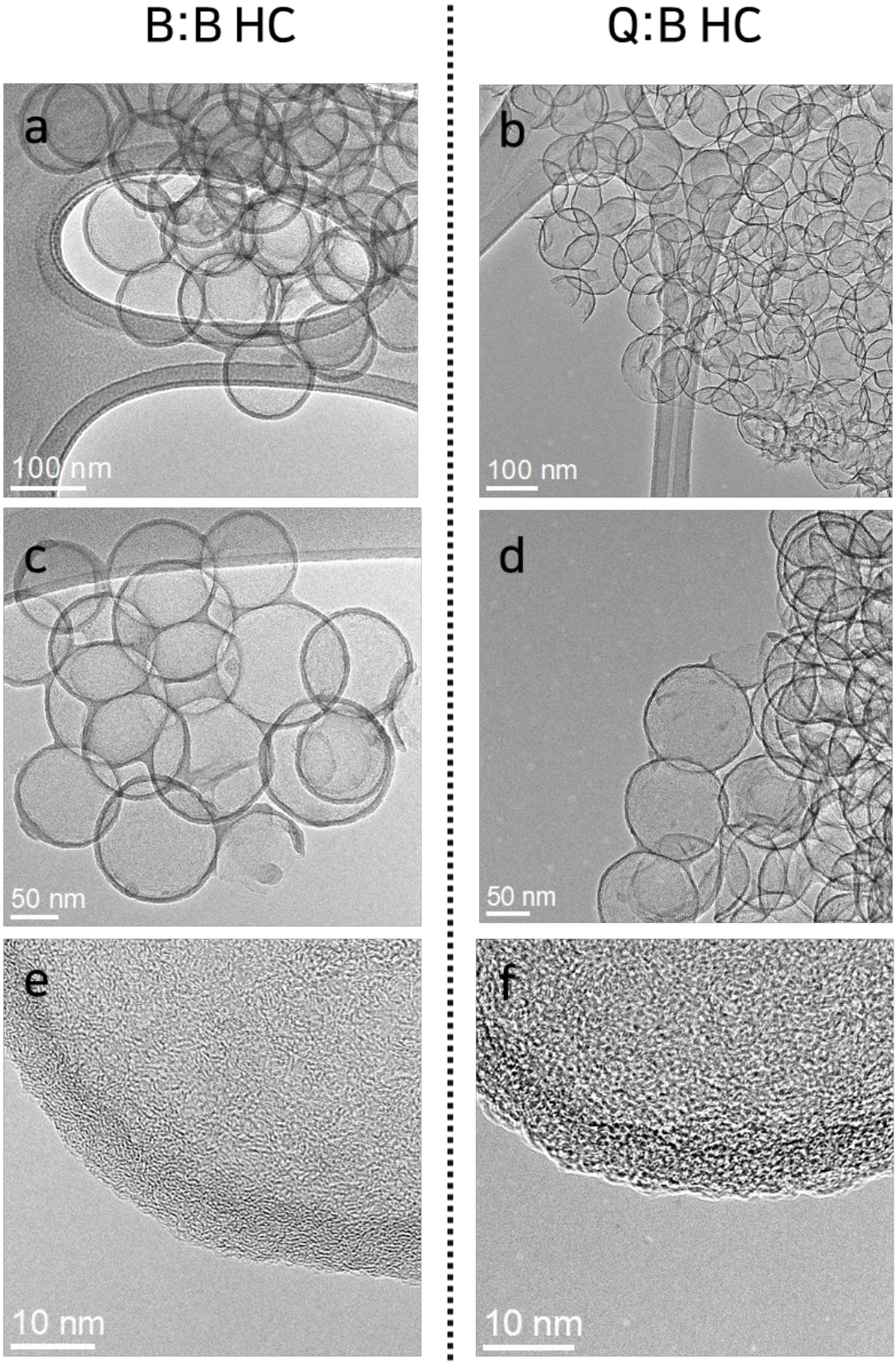

Figure S3 | TEM images. Those for B:B HC (**a**,**c**,**e**) and Q:B HC (**b**,**d**,**f**).

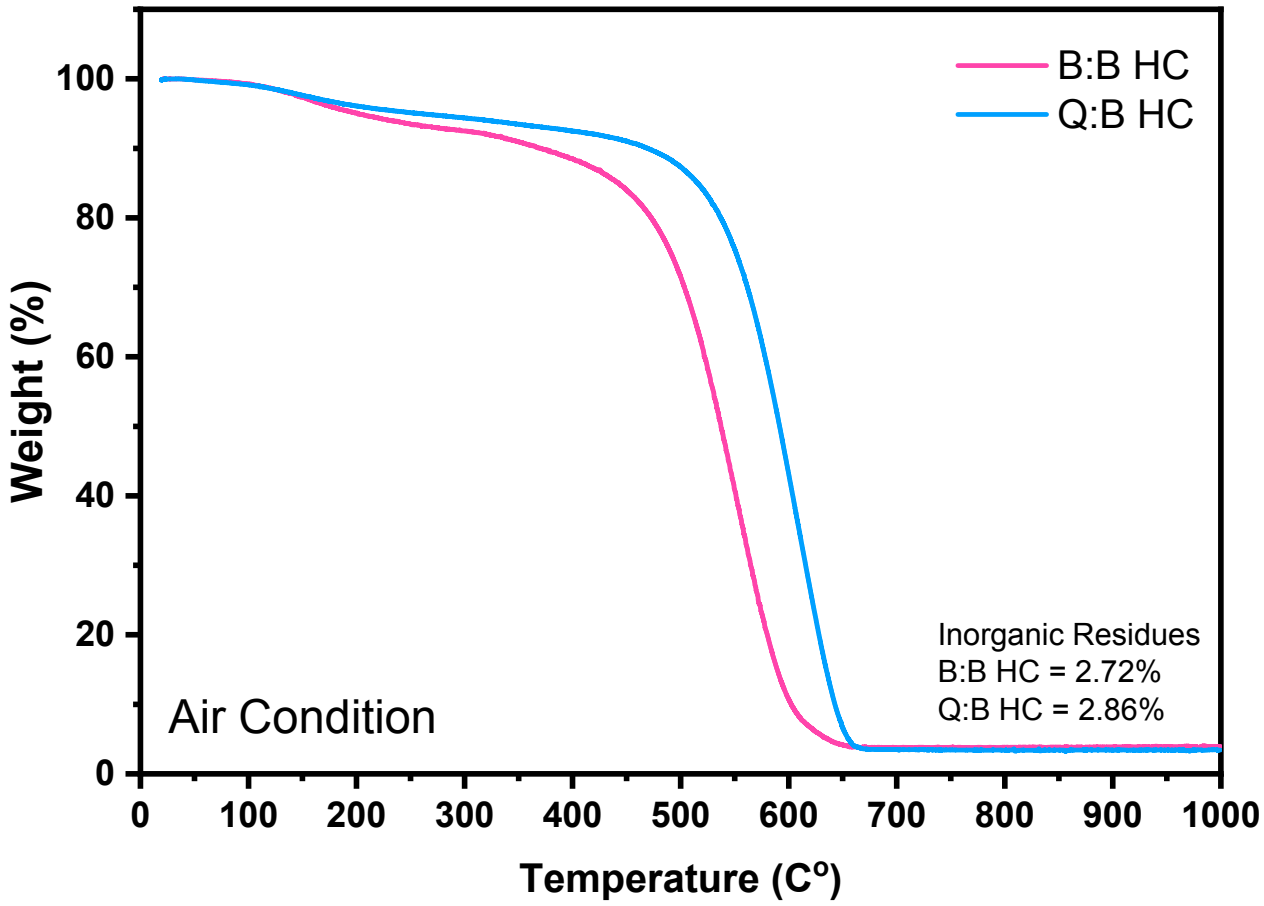

Figure S4 | TGA data of B:B HC and Q:B HC under air condition.

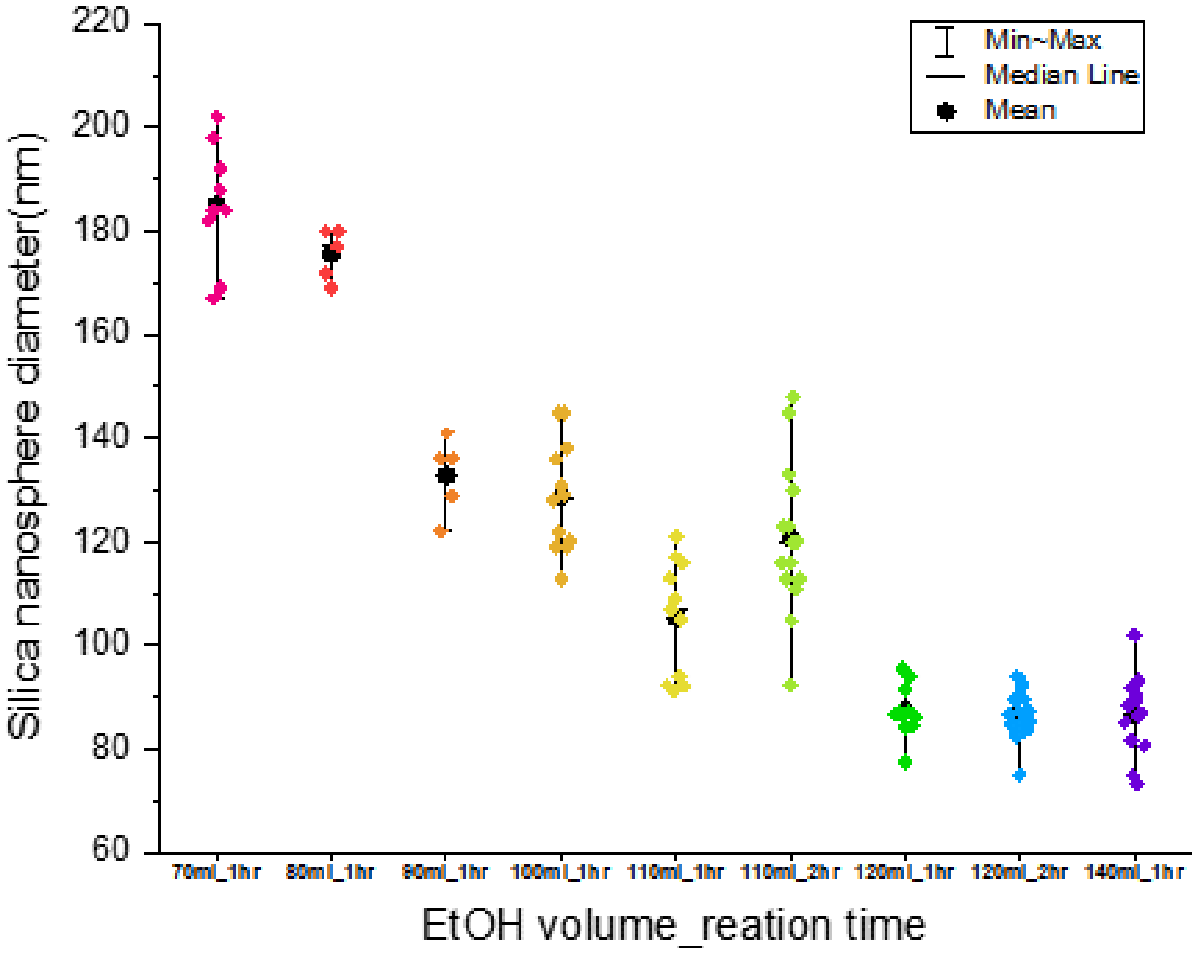

Figure S5 | Diameters of silica nanospheres controlled by varying the ethanol volume and reaction time conditions in Stöber process.

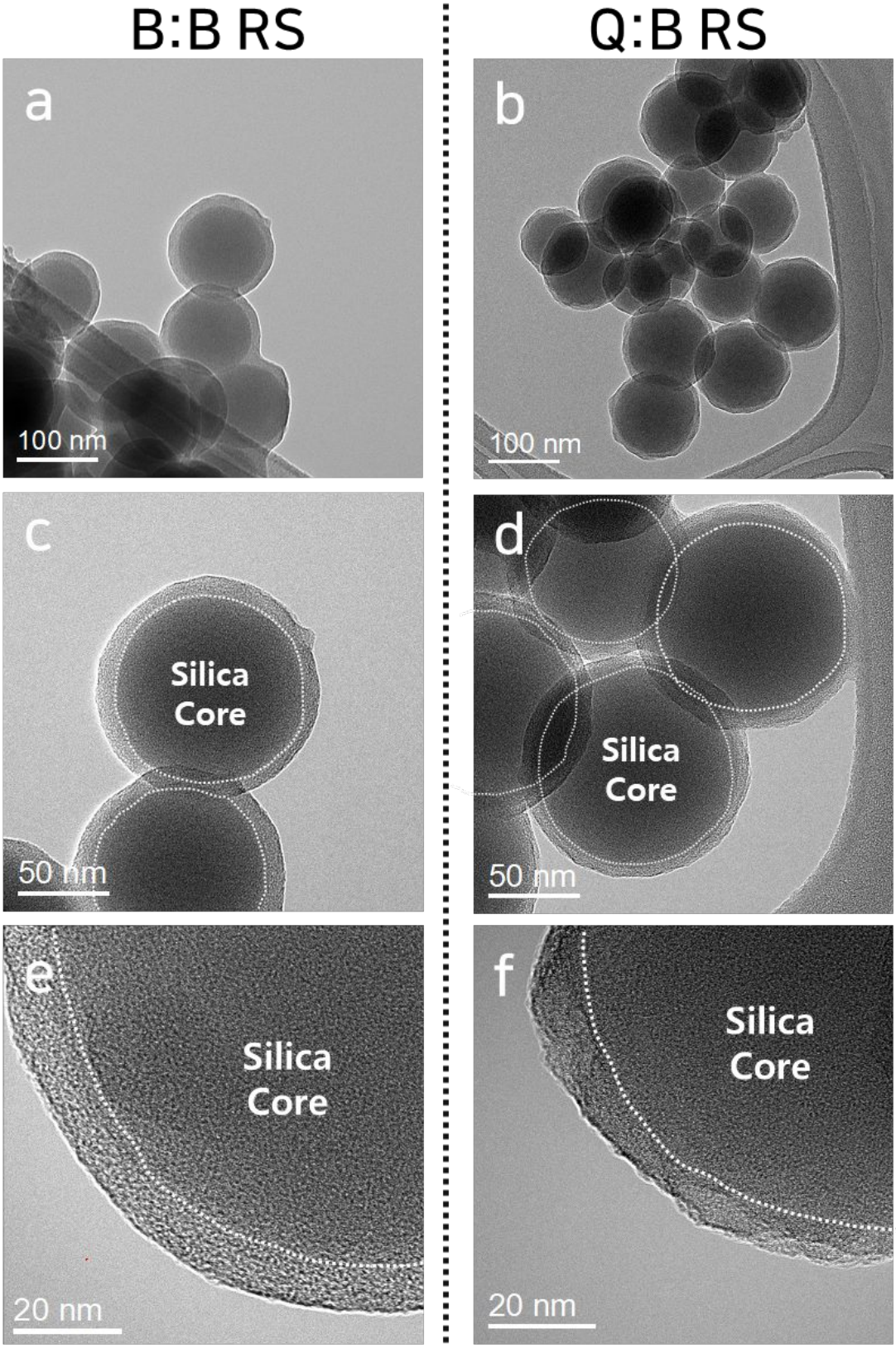

Figure S6. TEM images. Those for B:B RS (**a**,**c**,**e**) and Q:B RS (**b**,**d**,**f**). before carbonization and silica core etching processes.

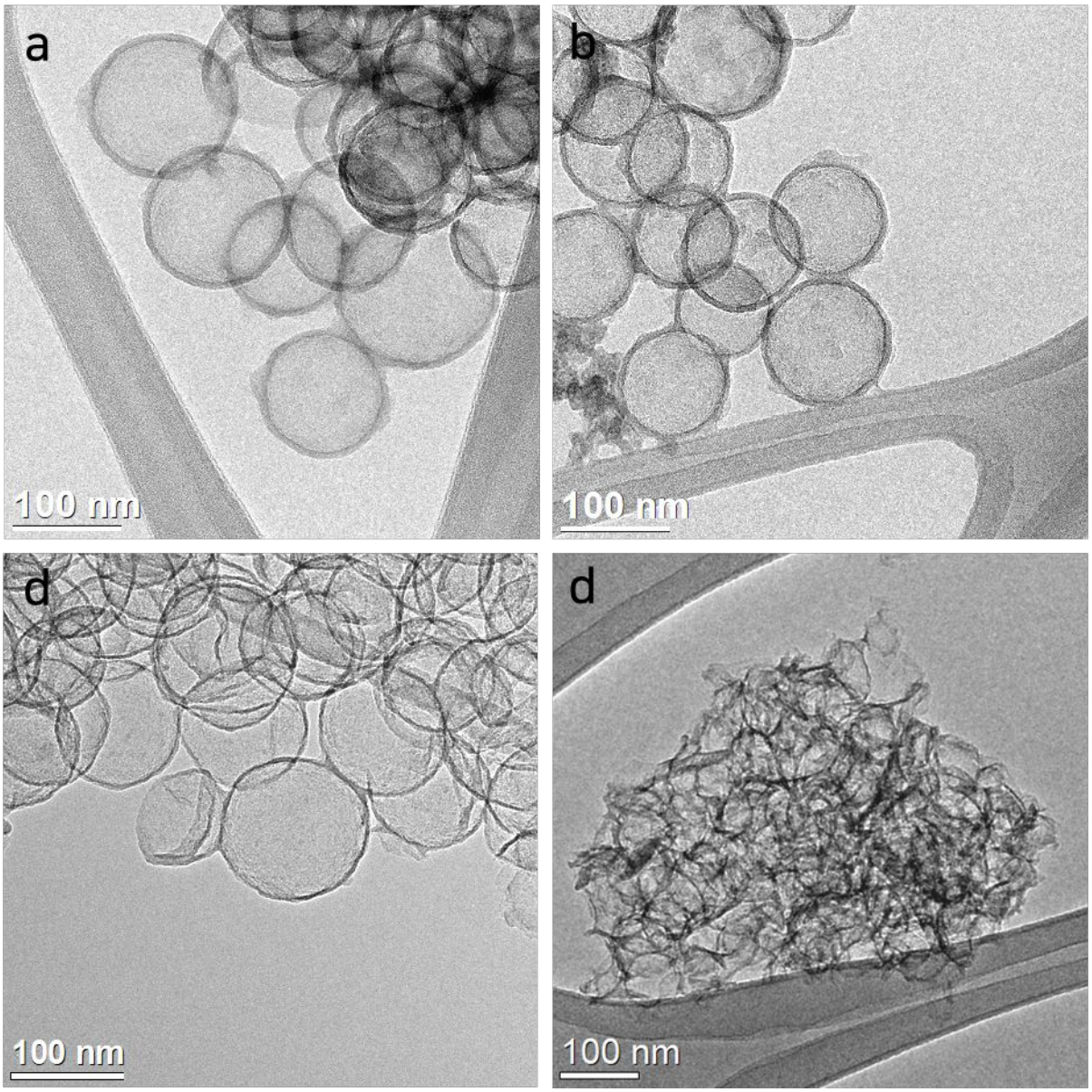

Figure S7 | TEM images of hollow carbons (HCs) synthesized using the different ratios of resorcinol and melamine.

Those for (**a**) melamine 20%, (**b**) melamine 40%, (**d**) melamine 60%, and (**d**) melamine 80%.

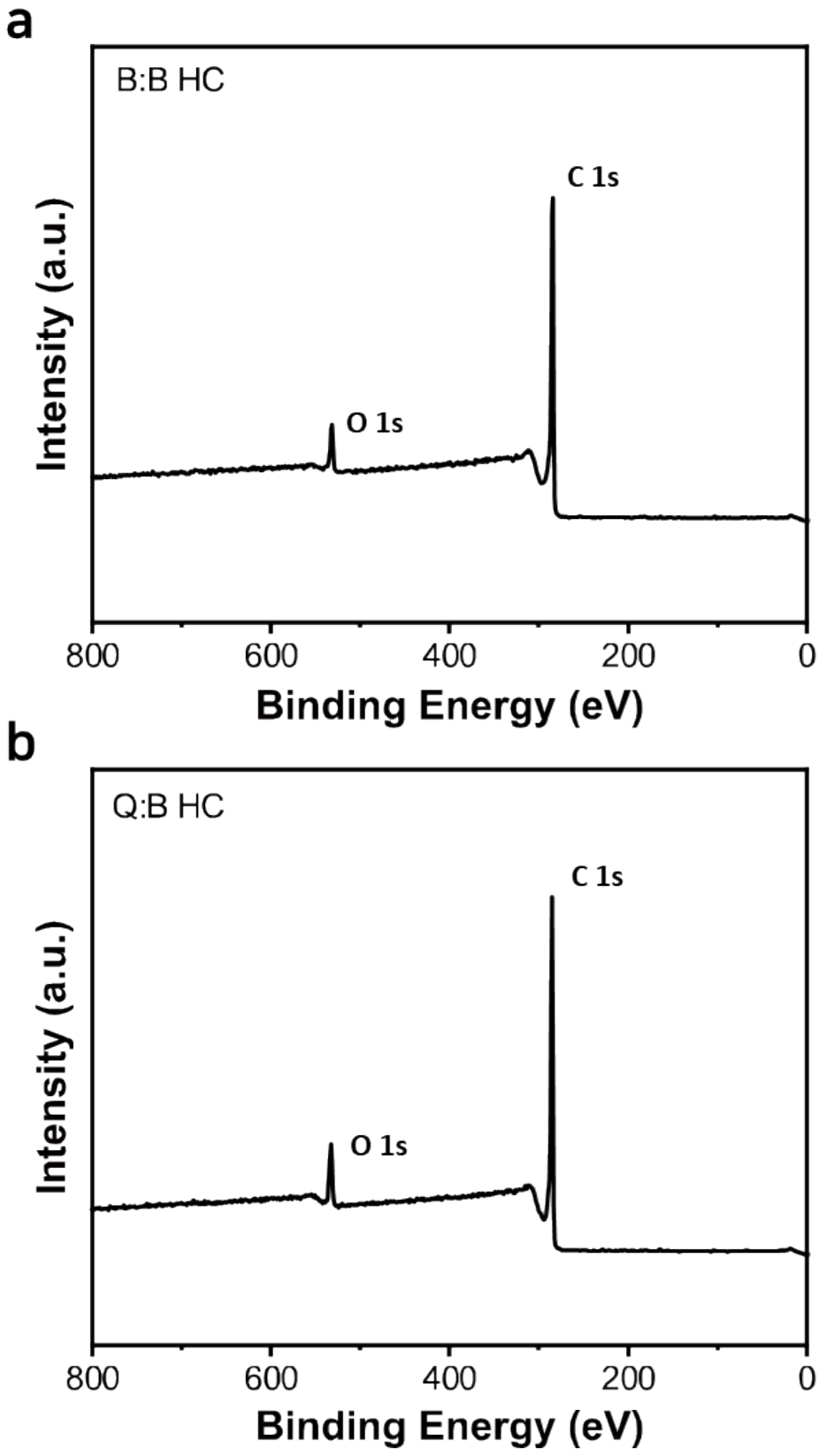

Figure S8 | XPS survey spectra. Those for (**a**) B:B HC and (**b**) Q:B HC.

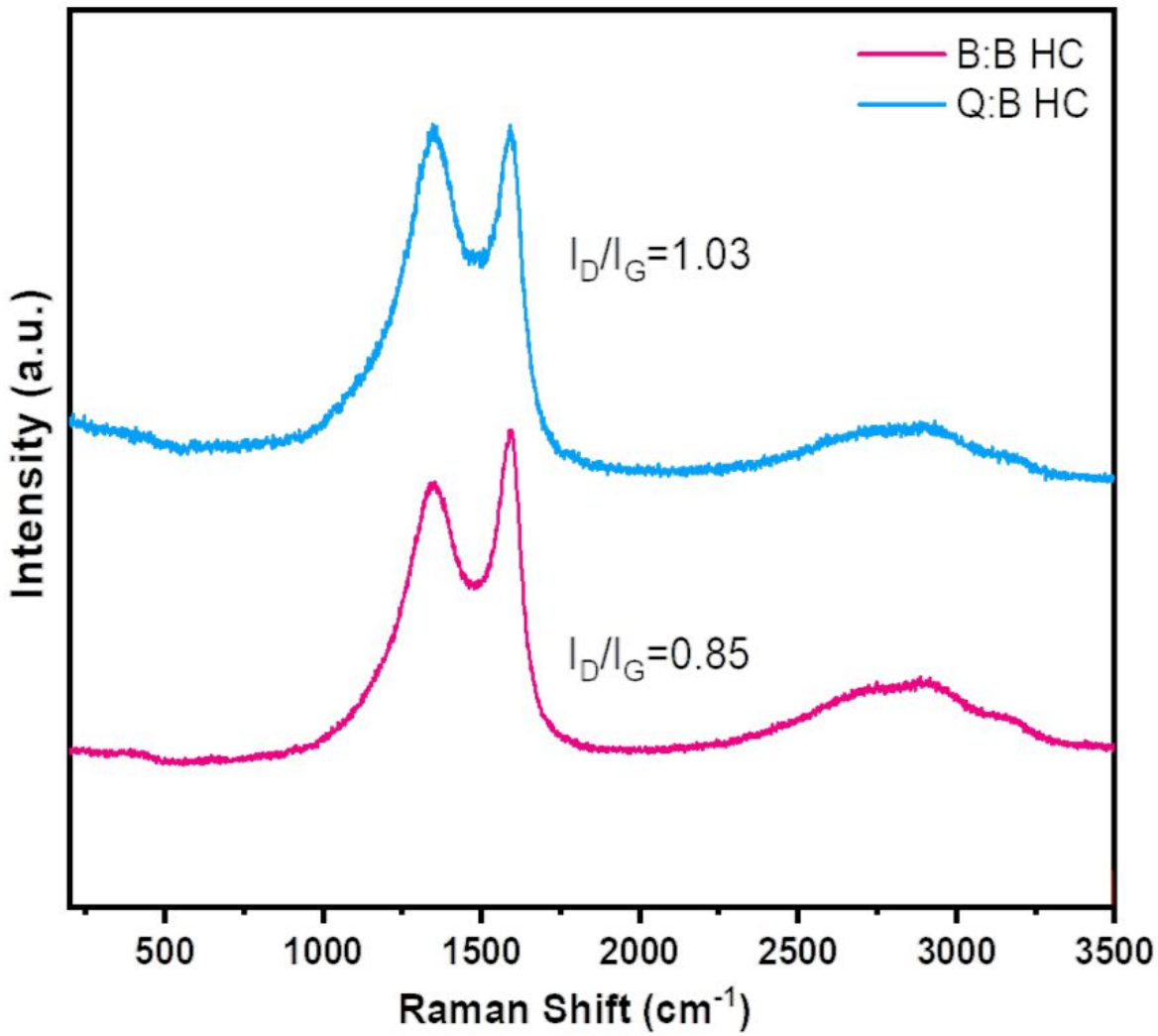

Figure S9 | Raman spectroscopy data of Q:B HC and B:B HC.

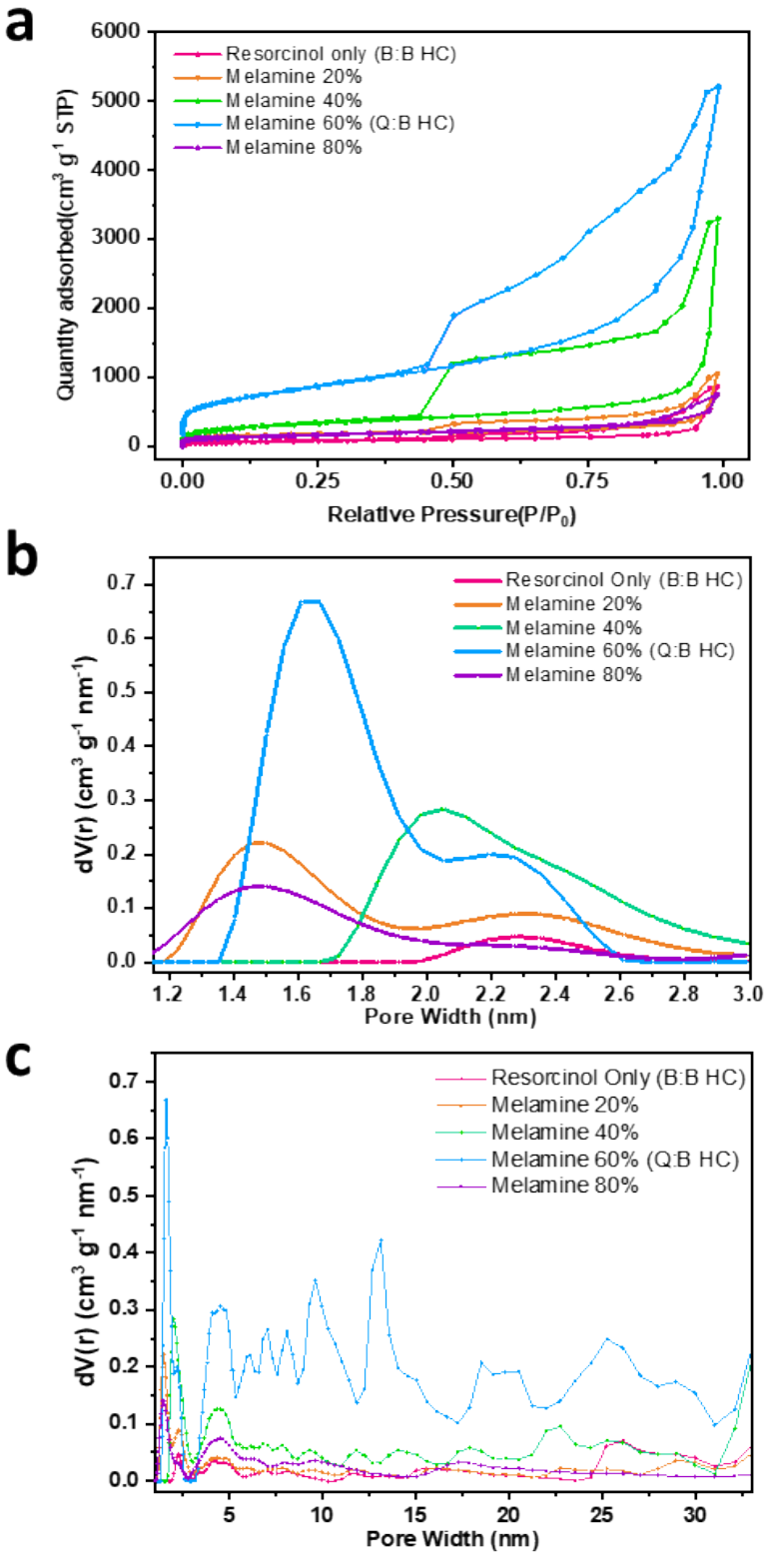
a
Resorcinol only (B:B HC)
Melamine 20%
Melamine 40%
Melamine 60% (Q:B HC)
Melamine 80%
Quantity adsorbed(cm3 g-1 STP)
Relative Pressure(P/P0)
b
Resorcinol Only (B:B HC)
Melamine 20%
Melamine 40%
Melamine 60% (Q:B HC)
Melamine 80%
dV(r) (cm3 g-1 nm-1)
Pore Width (nm)
c
Resorcinol Only (B:B HC)
Melamine 20%
Melamine 40%
Melamine 60% (Q:B HC)
Melamine 80%
dV(r) (cm3 g-1 nm-1)
Pore Width (nm)

Figure S10 | Nitrogen adsorption/desorption isotherms, micropores, and mesopores. (**a**) Nitrogen adsorption/desorption isotherm curves at 77K. (**b**) Micropore and (**c**) mesopore range pore distributions of HC samples with different melamine contents in precursors.

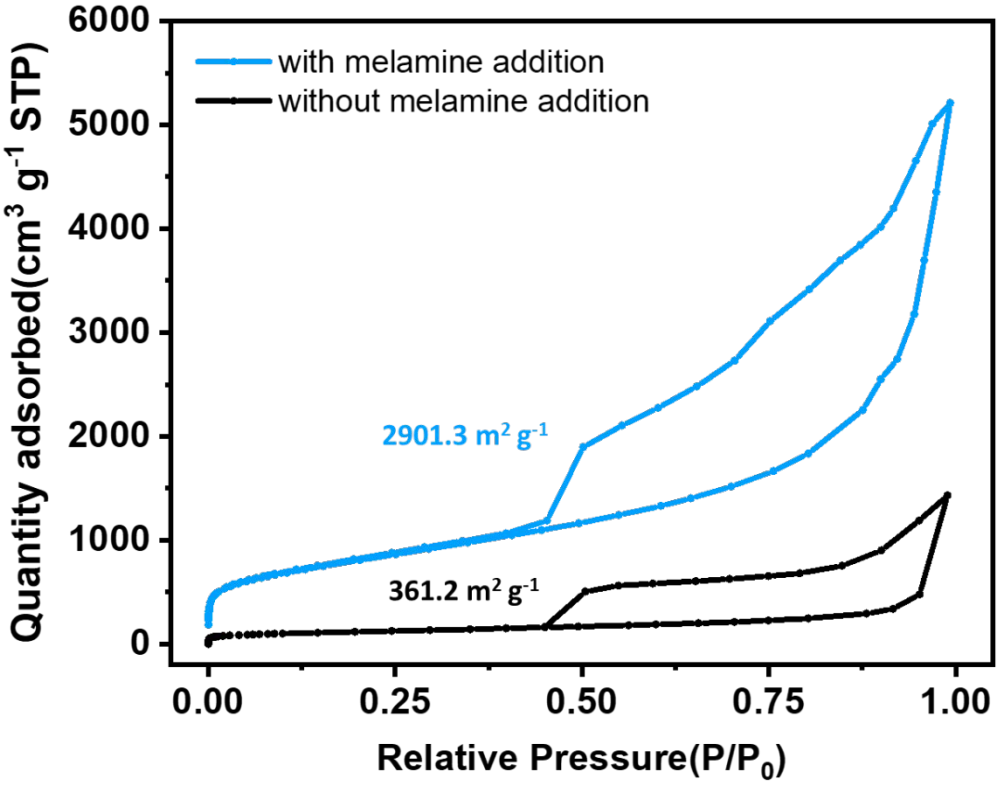

Figure S11 | The nitrogen adsorption/desorption isotherm curves and specific surface area of same resorcinol amount derived HC with or without melamine addition at 77K.

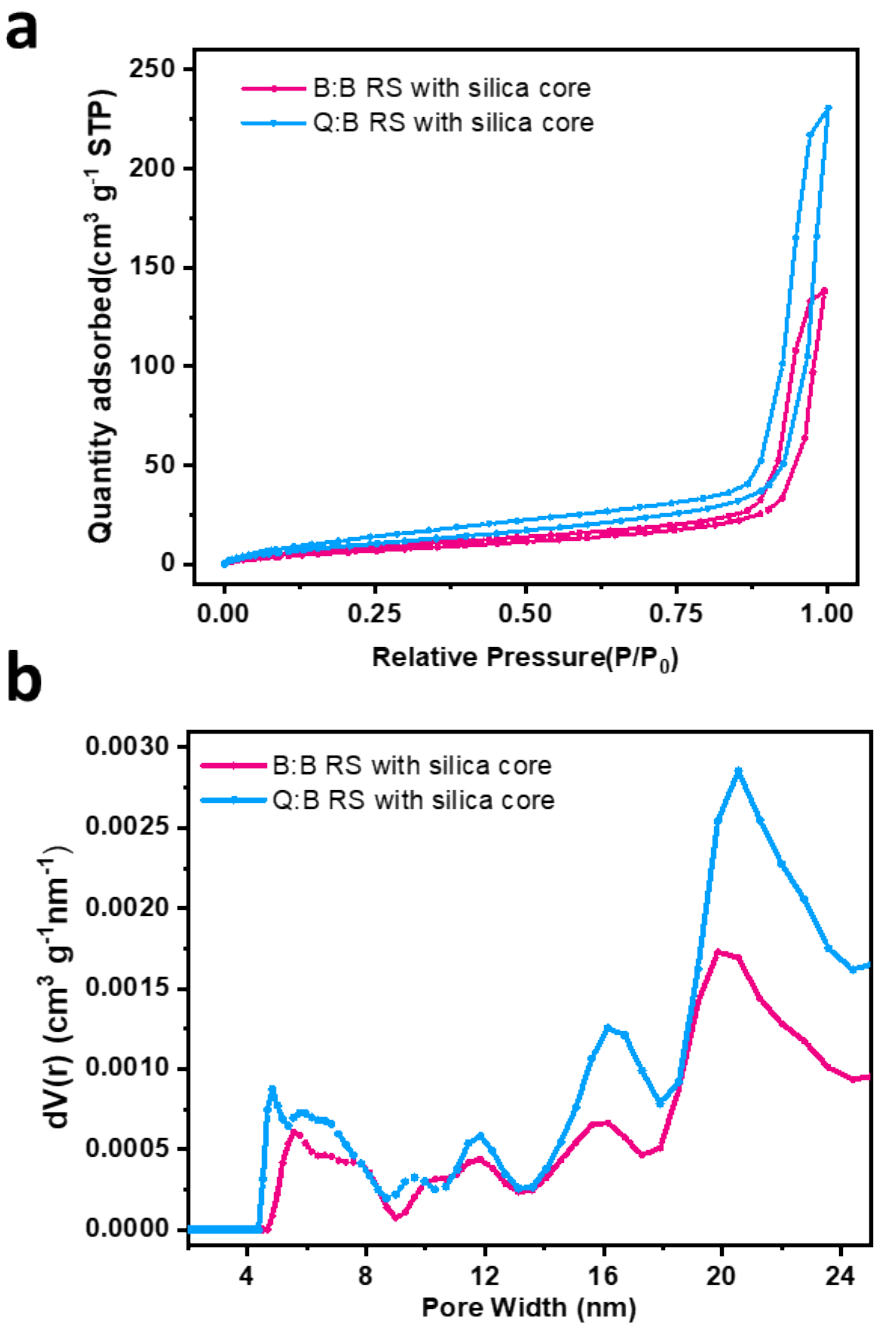

Figure S12 | Nitrogen adsorption/desorption isotherms and pore distributions. (**a**) Nitrogen adsorption/desorption isotherm curve at 77K and (**b**) pore distribution curves of B:B RS and Q:B RS with silica cores.

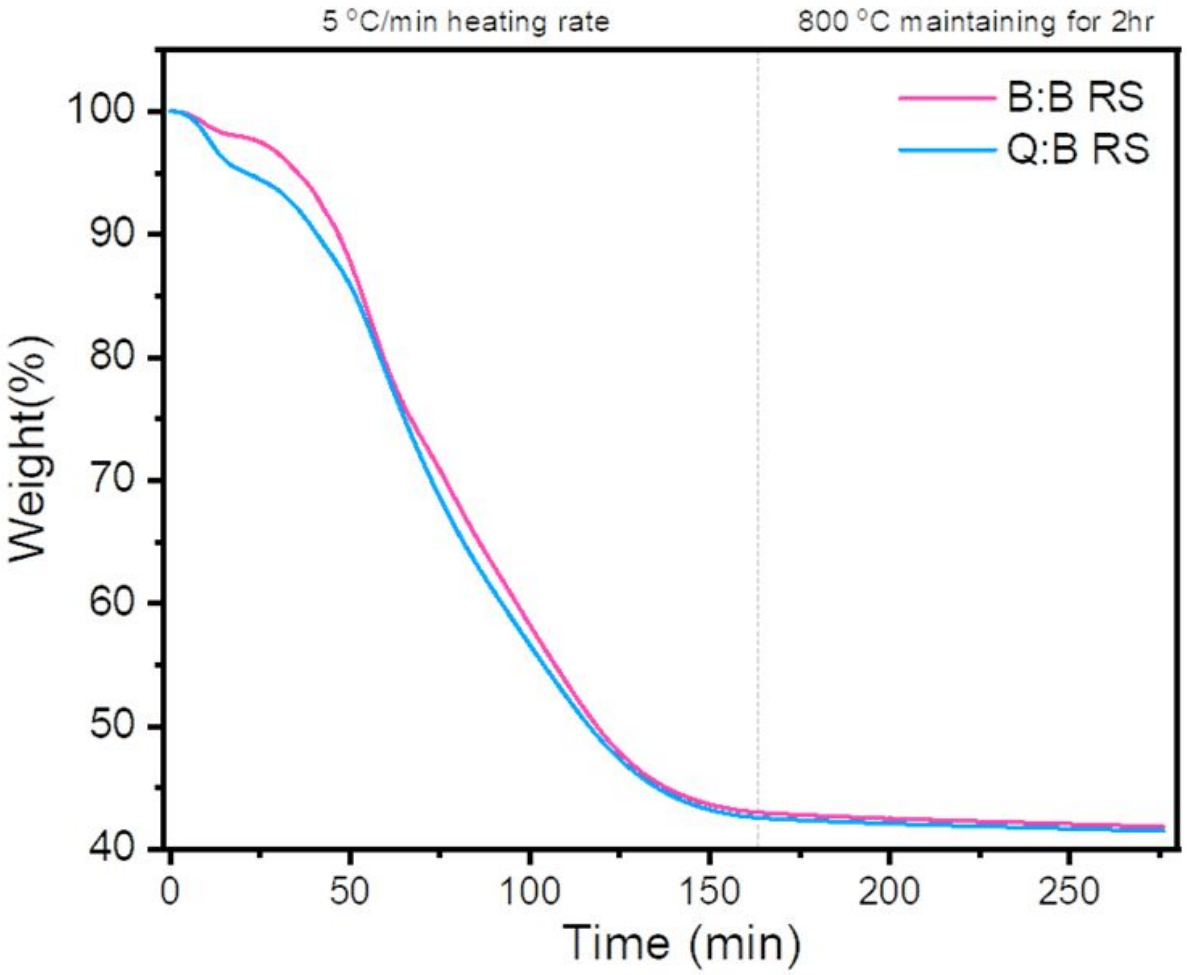

Figure S13 | TGA data of B:B RS and Q:B RS during the carbonization process under Ar atmosphere.

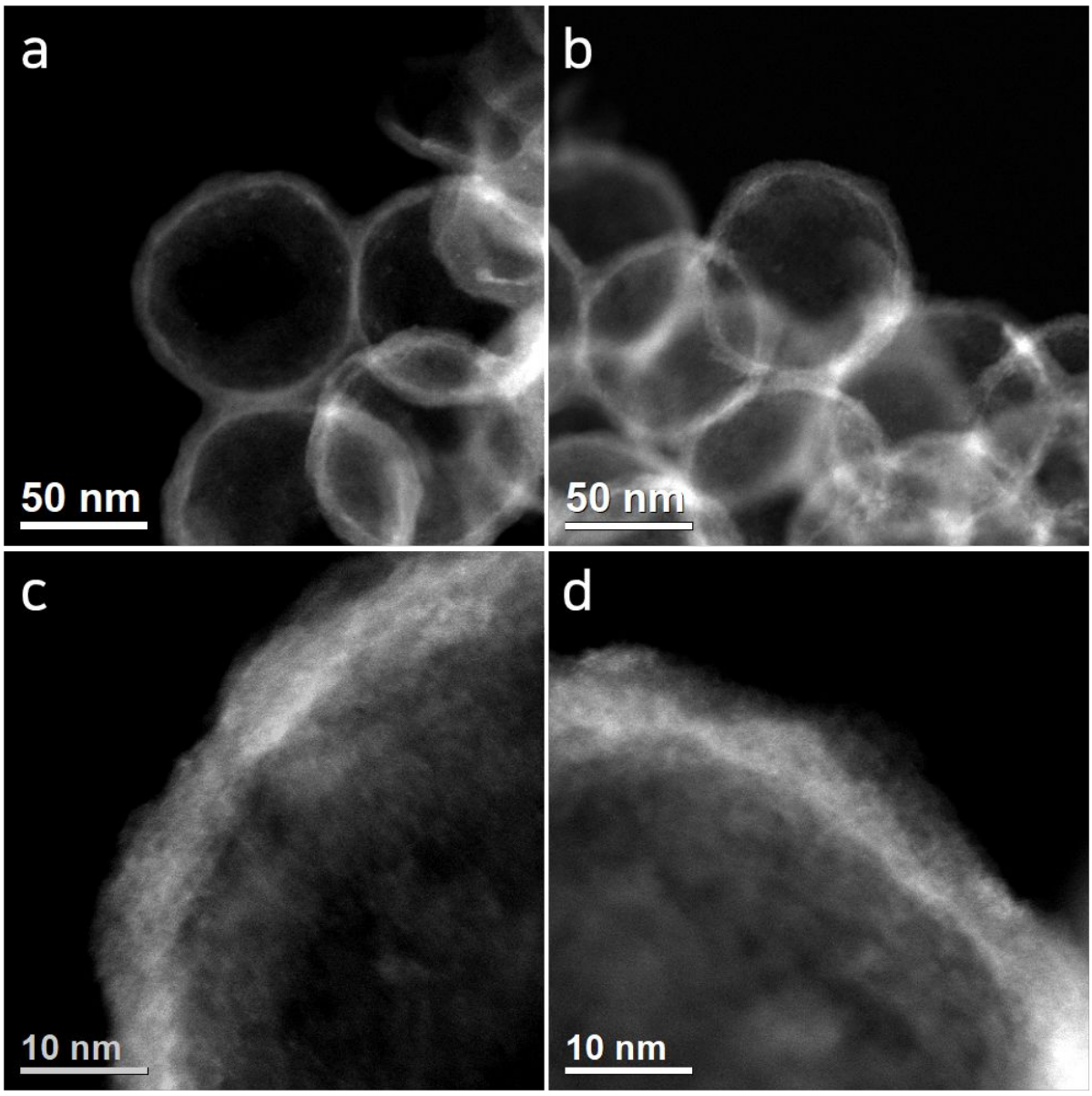

Figure S14 | HADDF-STEM images of Mono Ge-Q:B HC on different magnifications. 50-nm scale bars (**a**,**b**) and 10-nm scale bars (**c**,**d**).

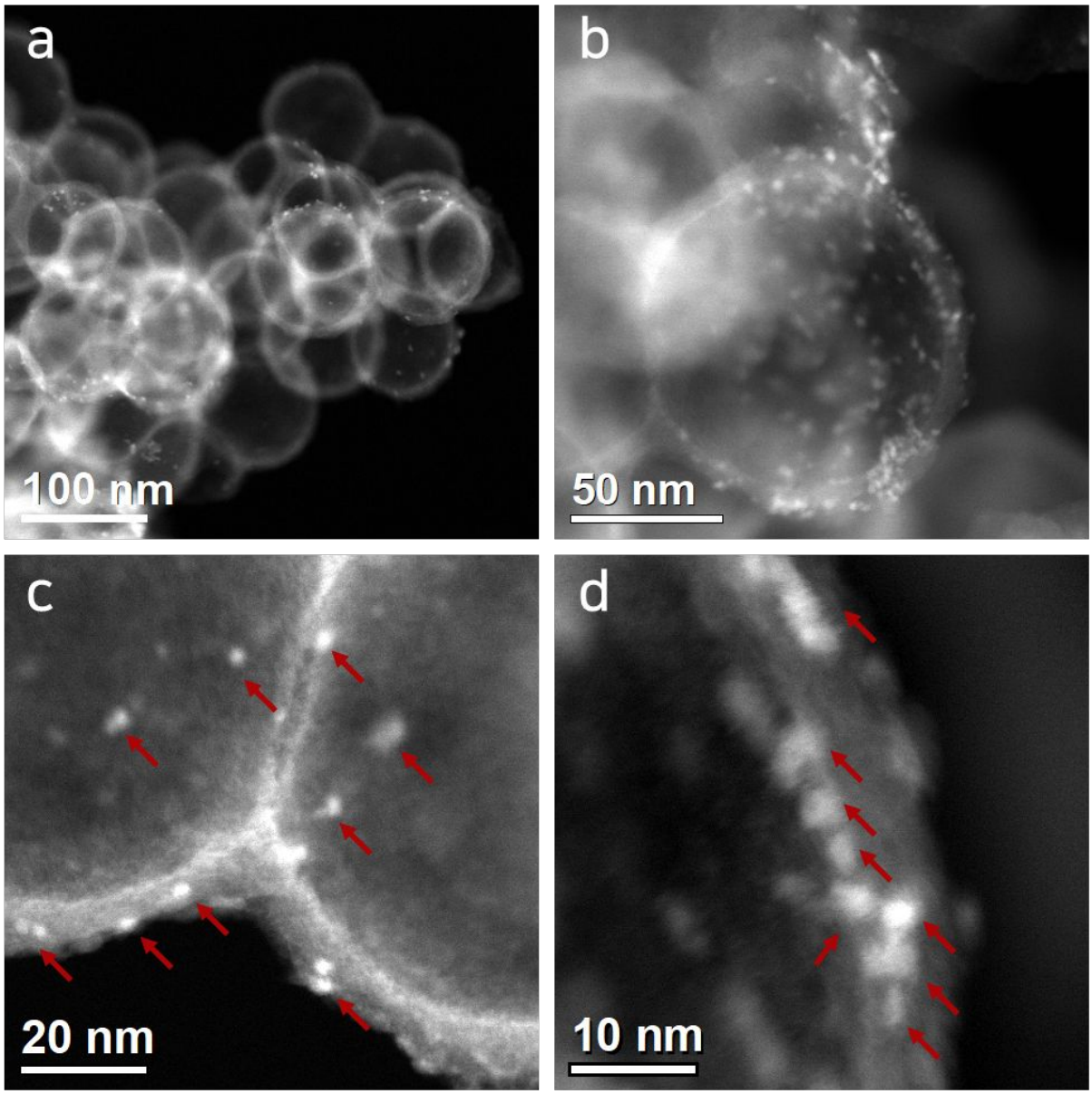

Figure S15 | HADDF-STEM images of Ge-Q:B HC derived from the intermediate Ge precursor concentration.

Different magnifications of (**a**) 100-nm scale bar, (**b**) 50-nm scale bar, (**c**) 20-nm scale bar, and (**d**) 10-nm scale bar, where nano-sized Ge particles are shown in red arrows.

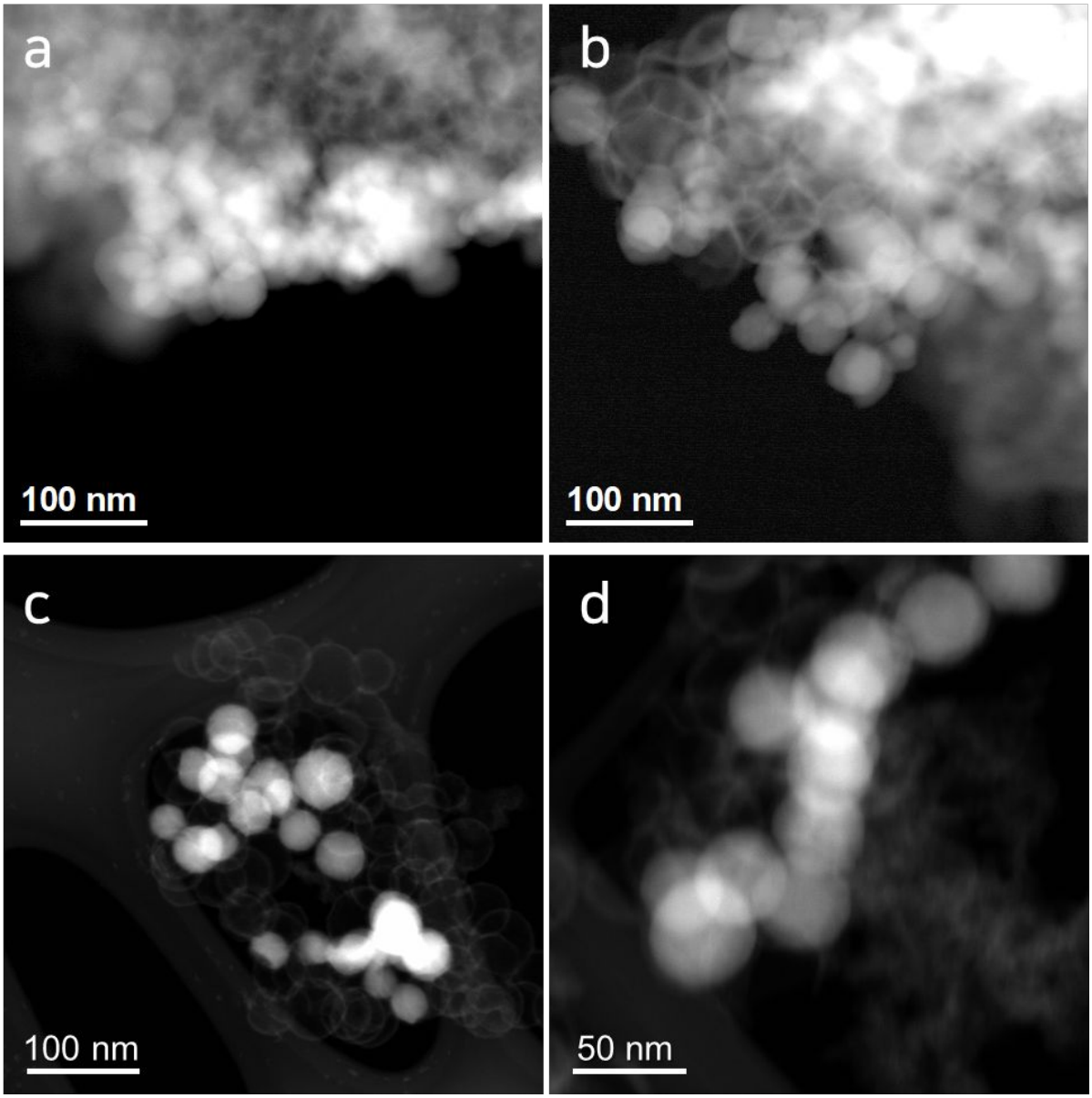

Figure S16 | HADDF-STEM images of Bulk Ge-Q:B HC having the aggregated bulk Ge particles. 100-nm scale bars (**a**,**b**,**c**) and 50-nm scale bar (**d**).

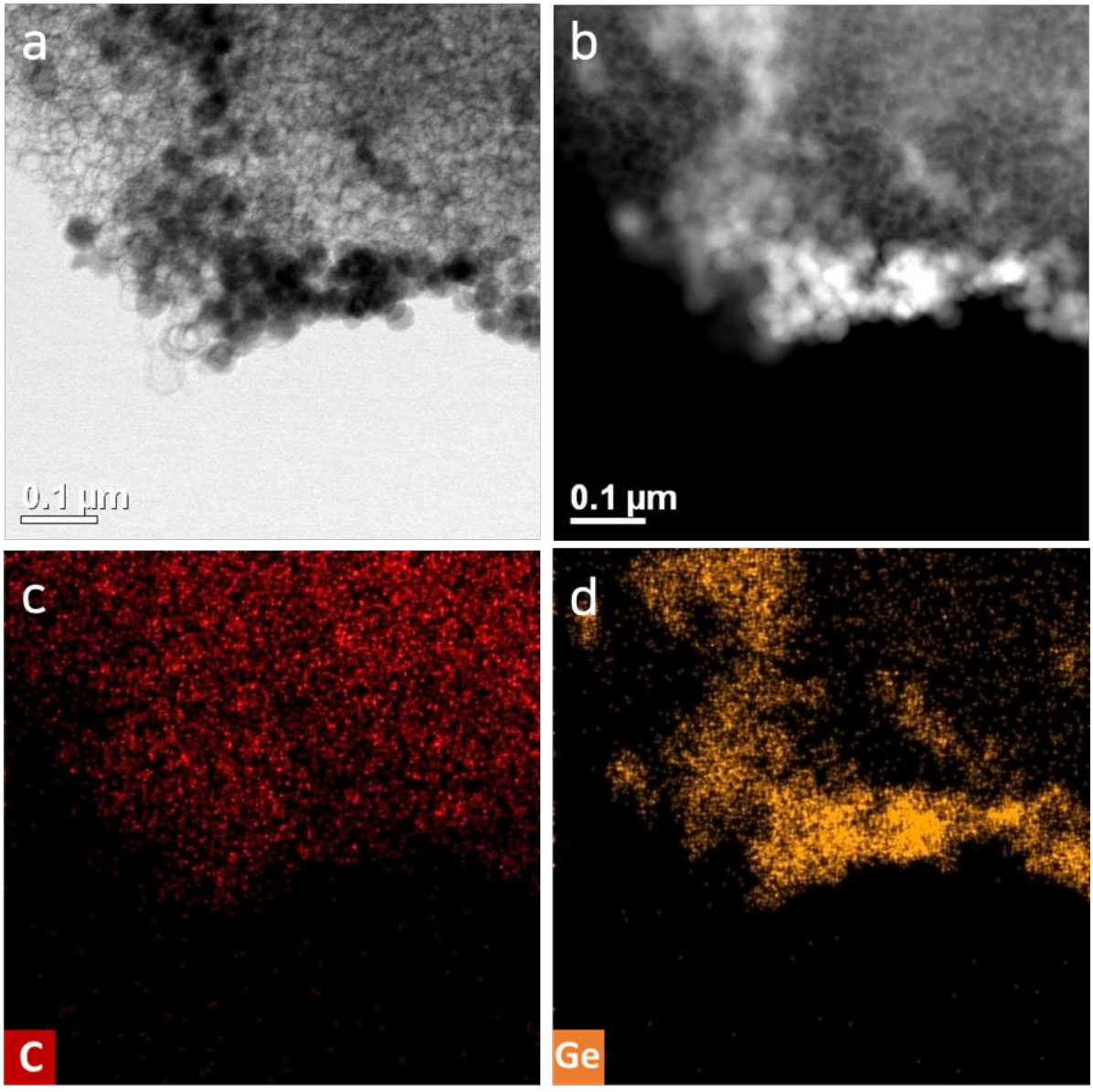

Figure S17 | TEM and EDS mapping images. of Bulk Ge-Q:B HC. (**a**) TEM image, (**b**) HADDF-STEM image, (**c**) Carbon EDS elemental mapping, and (**d**) Germanium EDS elemental mapping.

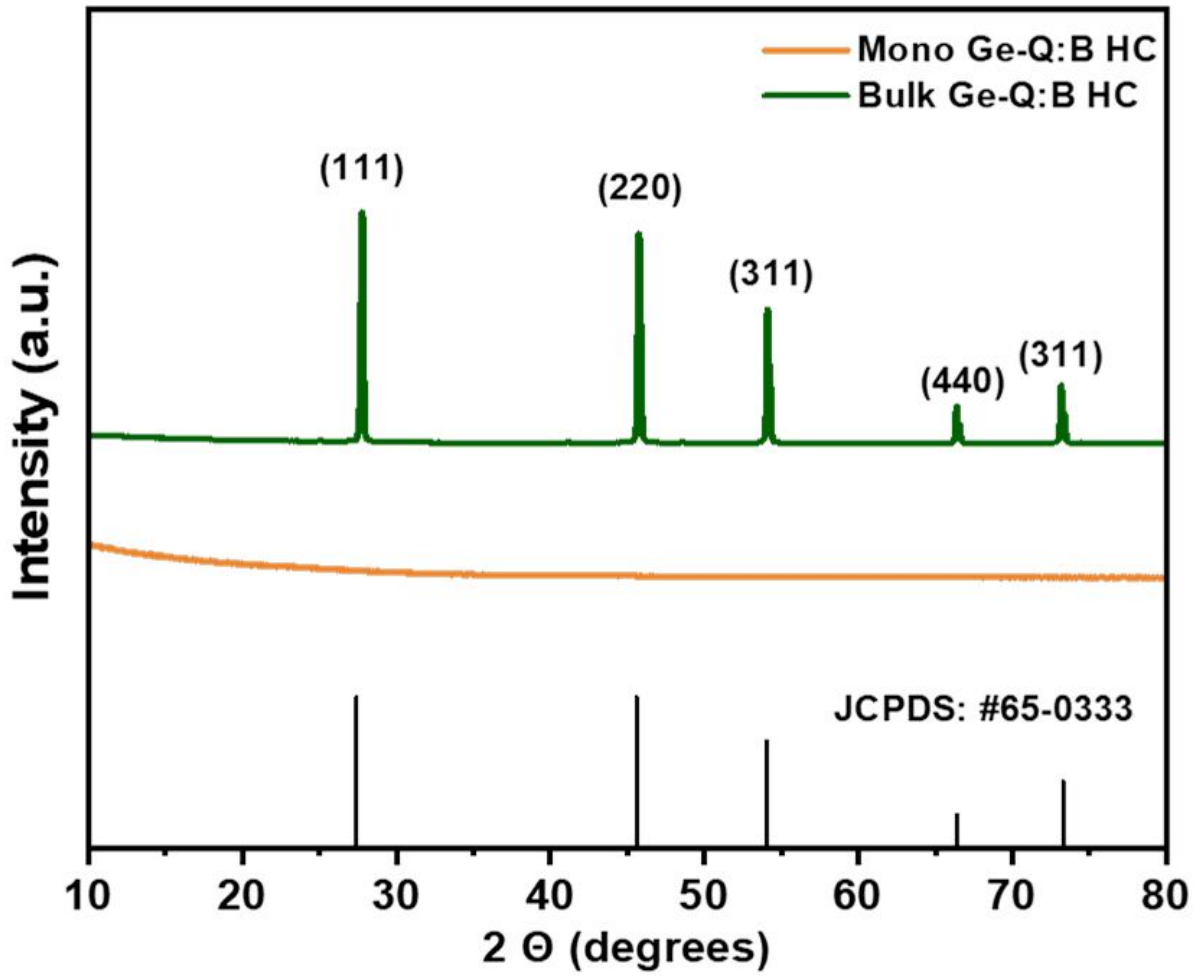

Figure S18 | XRD patterns of Mono Ge-Q:B HC and Bulk Ge-Q:B HC.

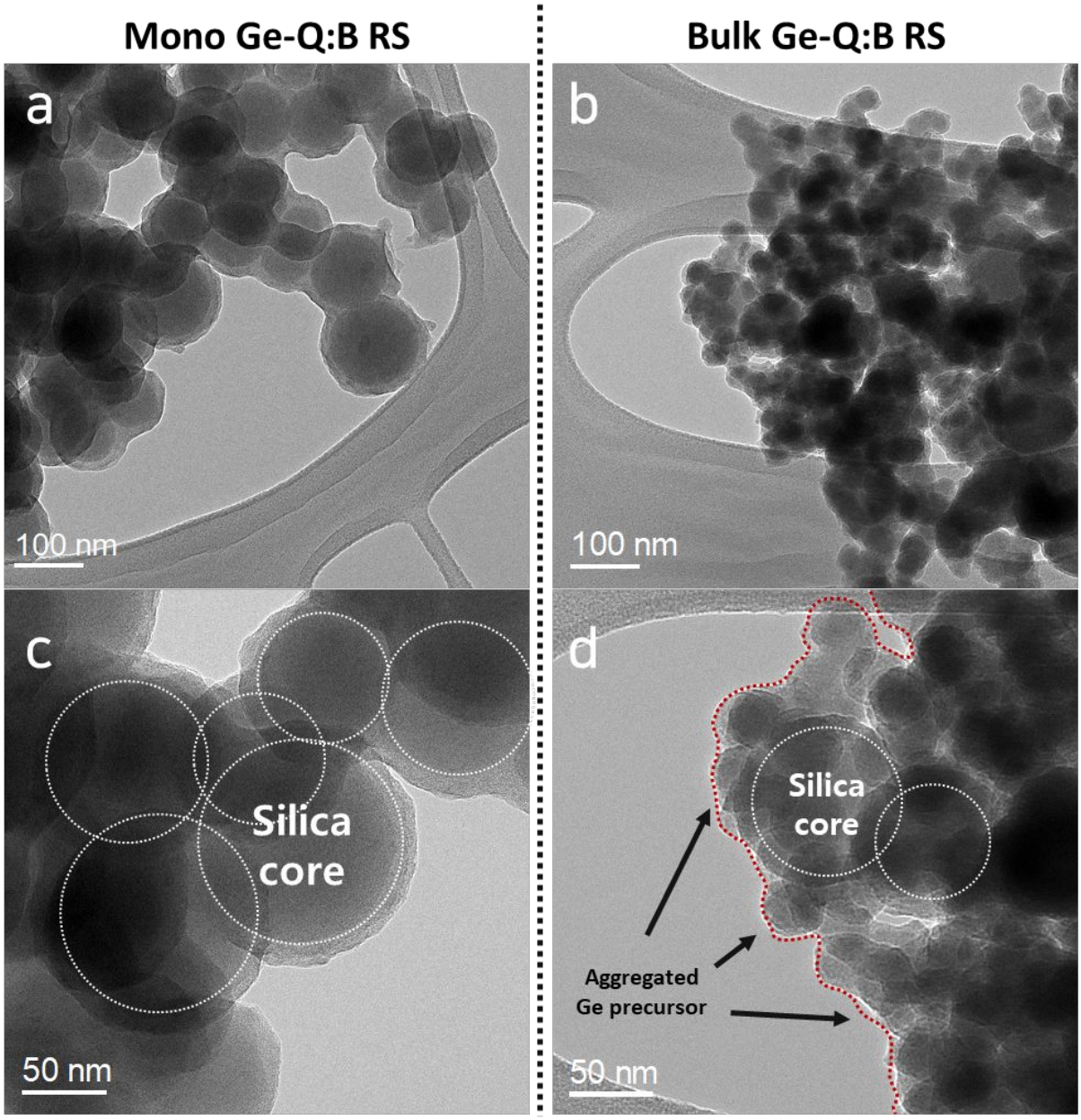

Figure S19 | TEM images of Mono Ge-Q:B RS and Bulk Ge-Q:B RS structures. Those for Mono Ge-Q:B RS (**a**,**c**) and Bulk Ge-Q:B RS (**b**,**d**) before carbonization and silica core etching processes.

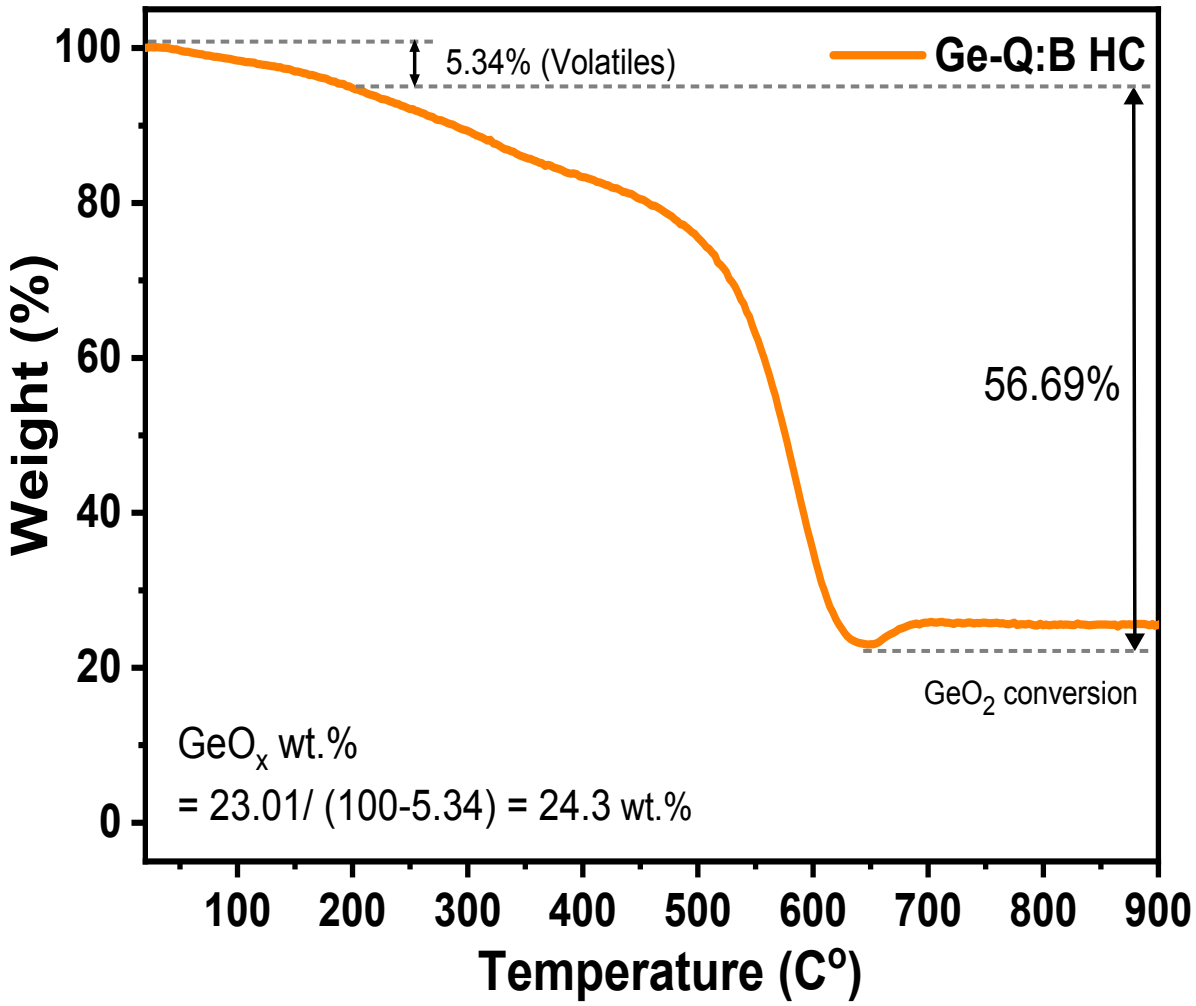

Figure S20 | TGA analysis in air atmosphere condition of Mono Ge-Q:B HC showing the calculated GeO_x weight percent.

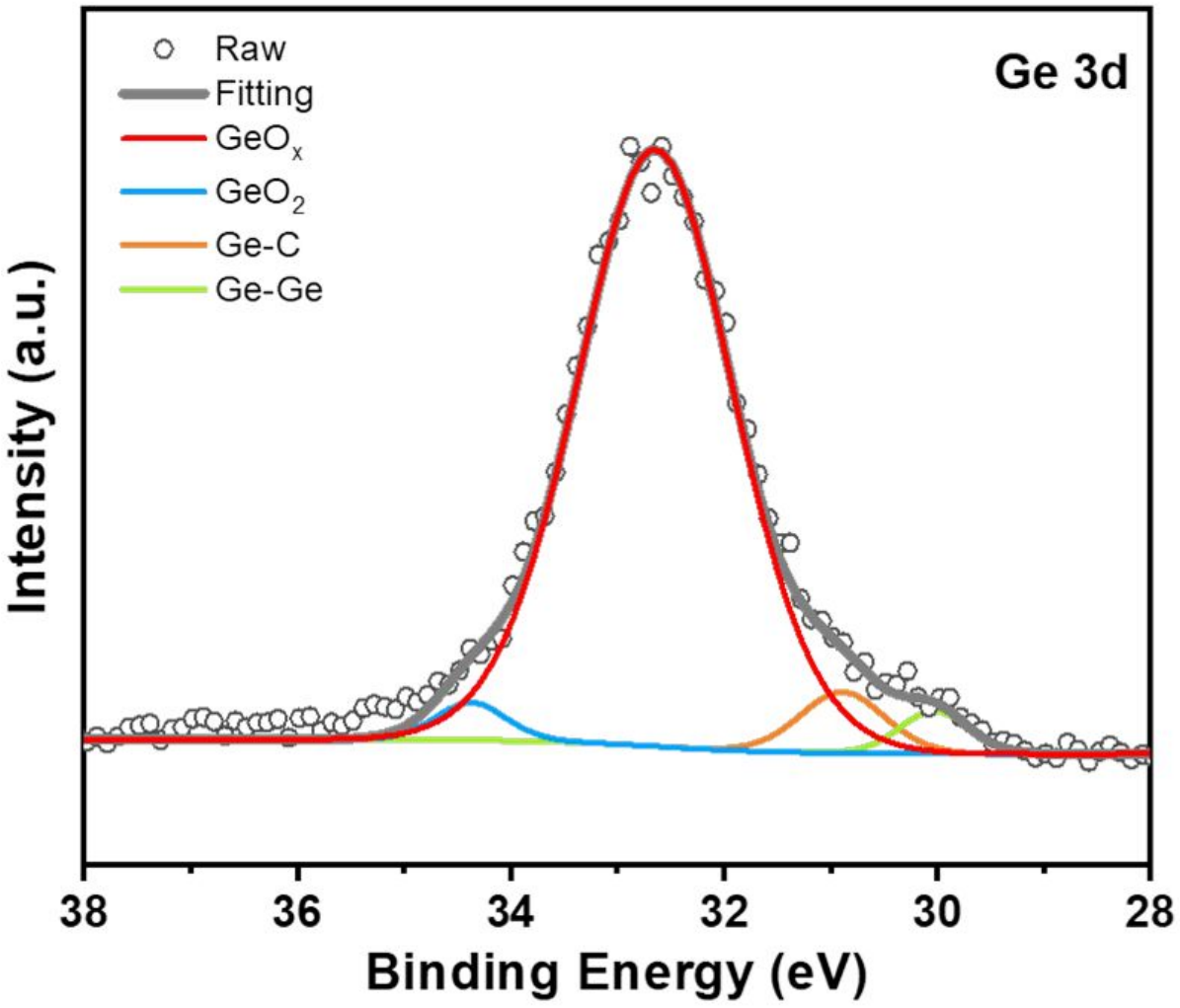

Figure S21 | XPS Ge 3d spectra of Mono Ge-Q:B HC.

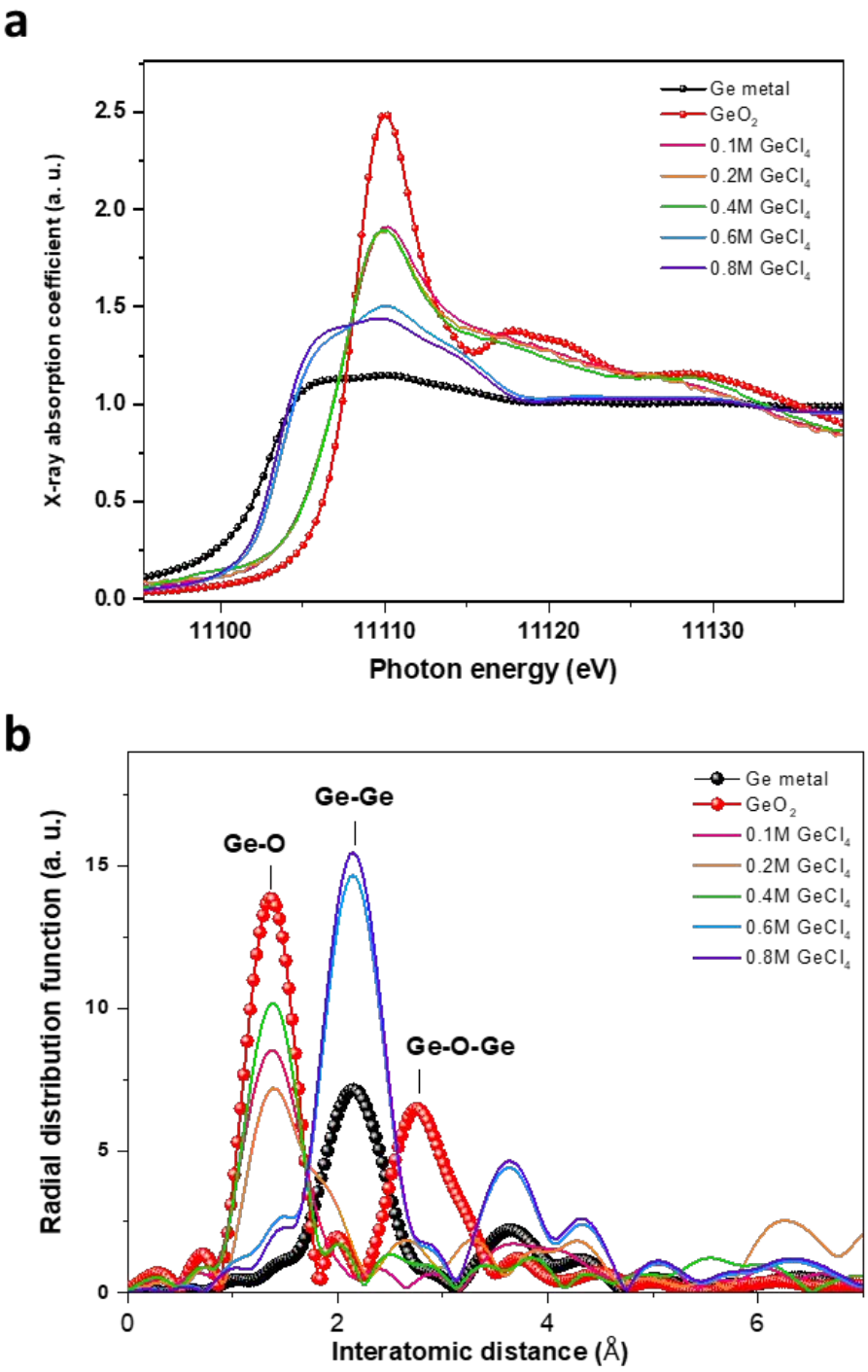

Figure S22 | X-ray absorption spectra. (a) XANES and (b) EXAFS of Ge-Q:B HC with the different Ge precursor concentrations.

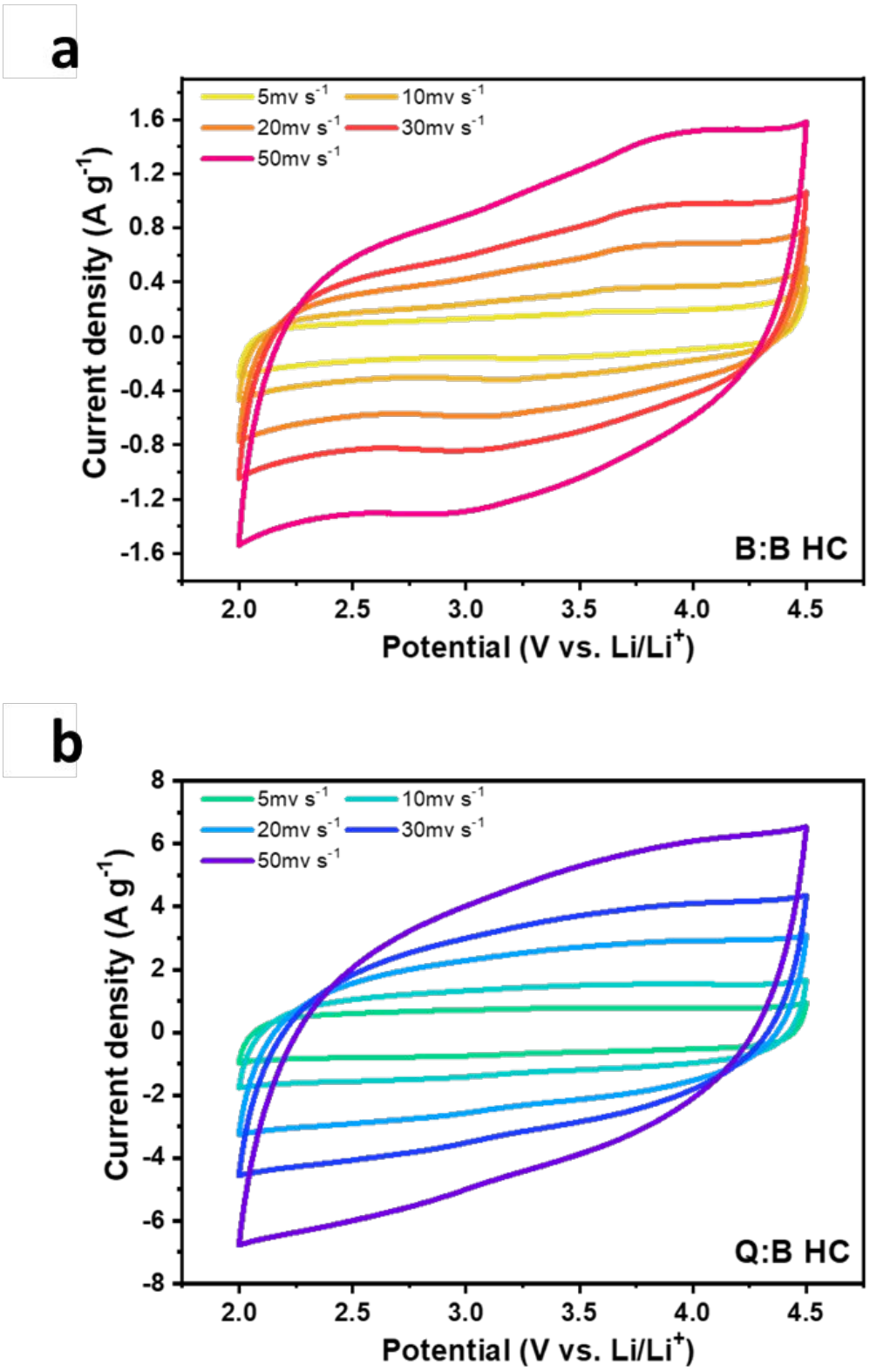

Figure S23 | CV curves of B:B HC (a) and Q:B HC (b) with the different scan rates from 5 mv s^{-1} to 50 mv s^{-1}.

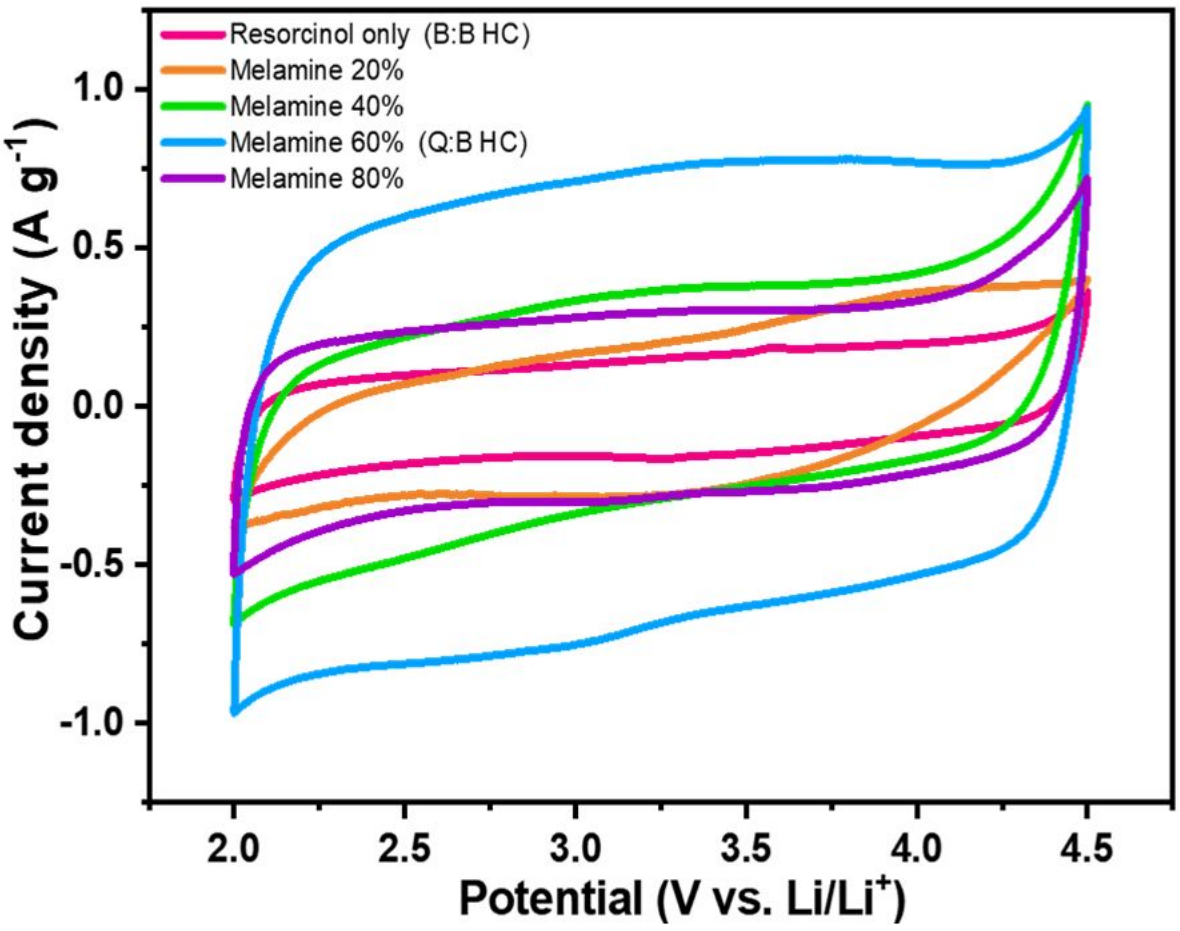

Figure S24 | 10mv s^{-1} scan rate CV curves of samples derived from the different melamine contents.

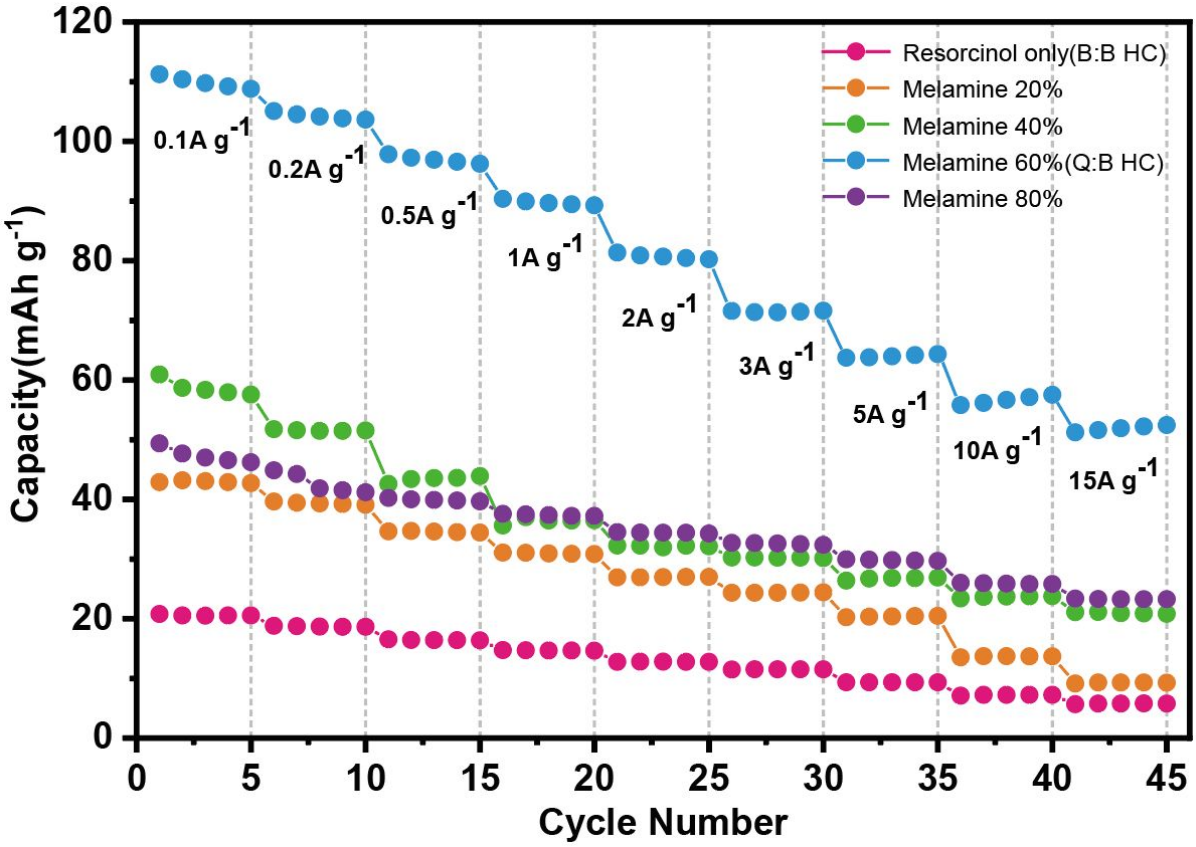

Figure S25 | Specific capacities of HC samples derived from the different melamine contents.

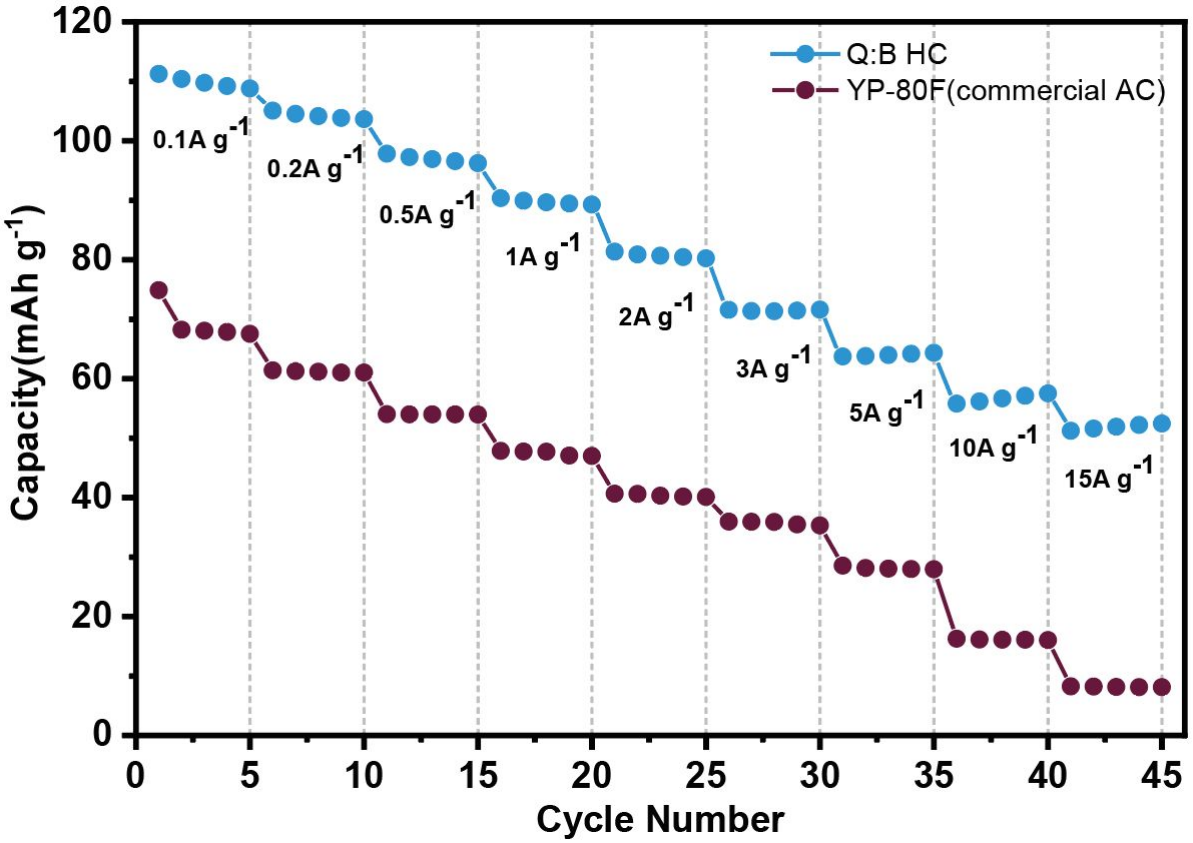

Figure S26 | Specific capacities comparison of Q:B HC and YP-80F commercial activated carbon.

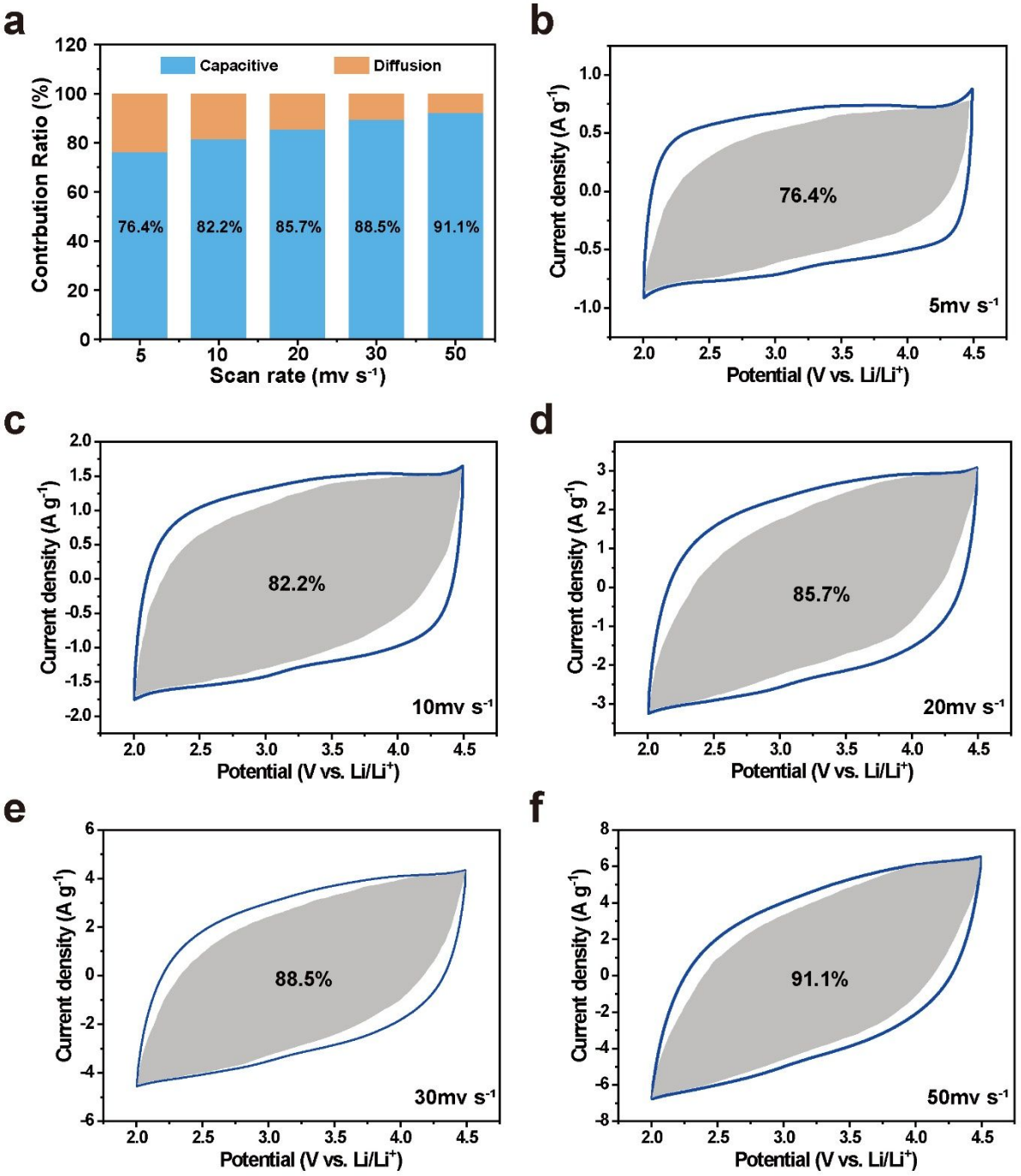

Figure S27 | Energy storage contribution ratios of Q:B HC cathode. (a) Capacitive (blue) and diffusion-controlled (orange) contributions at each scan rate of Q:B HC cathode and (b-f) CV curves of Q:B HC in each scan rates, where capacitive contribution area part (grey area) was determined from k_1 and k_2 values.

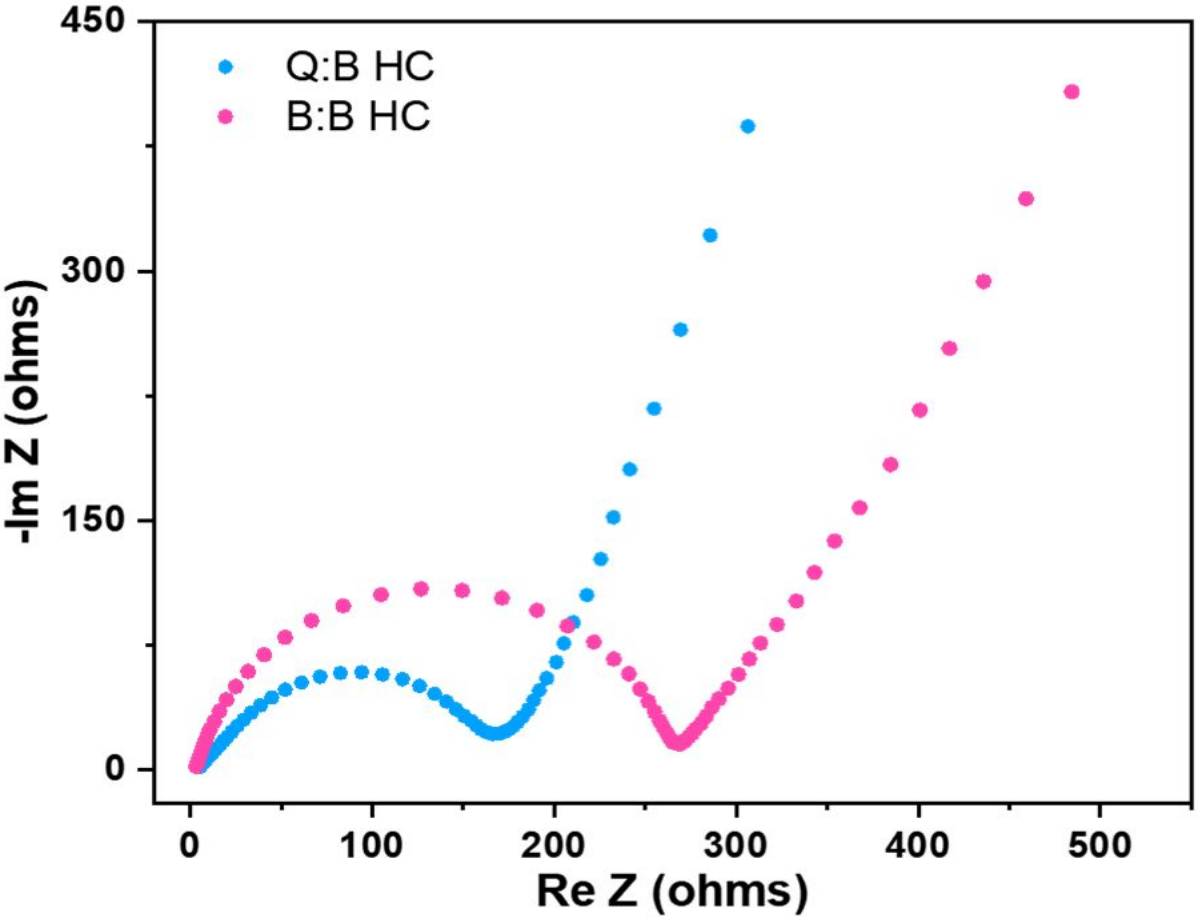

Figure S28 | Nyquist plots of Q:B HC and B:B HC under the open circuit voltage(OCV) state condition.

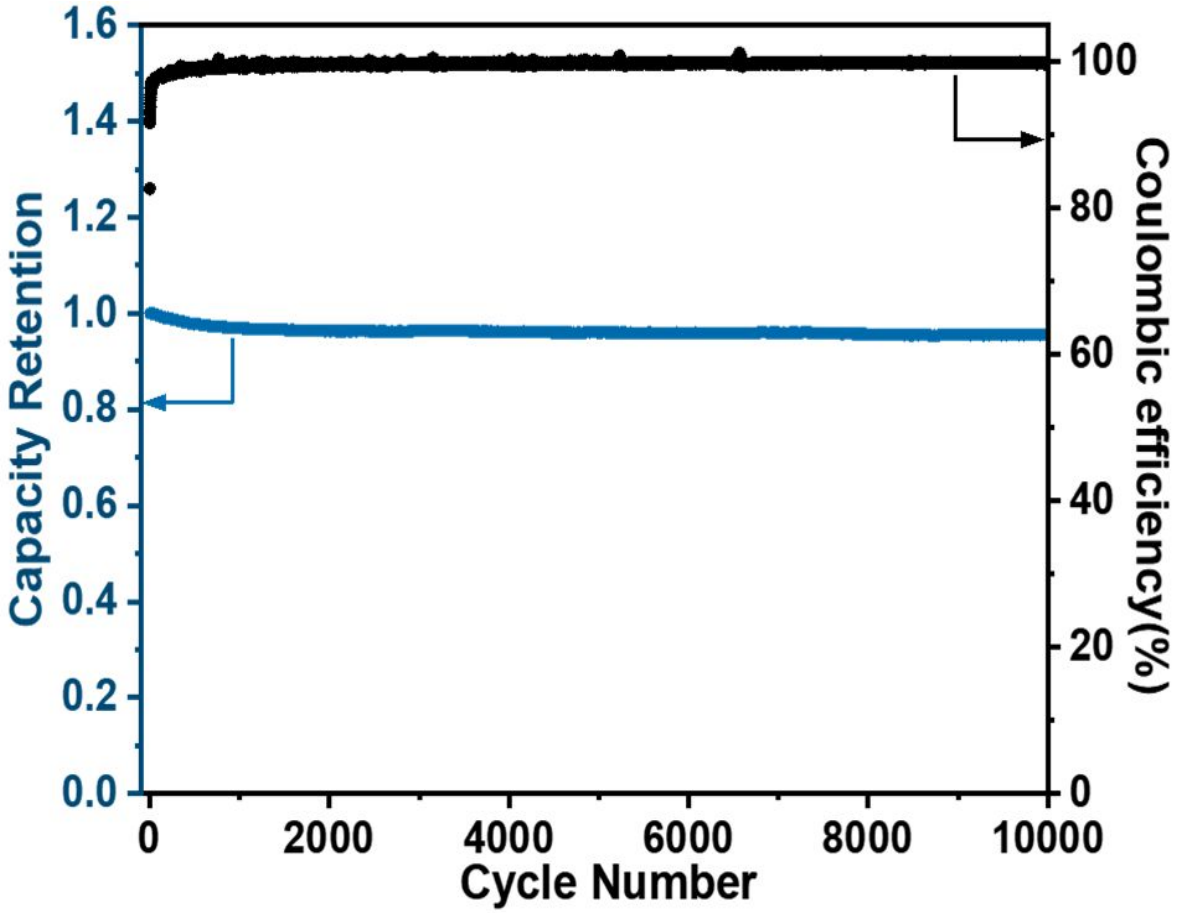

Figure S29 | Cycling stability over 10,000 cycles and coulombic efficiency of Q:B HC at the 2A g^{-1} current density.

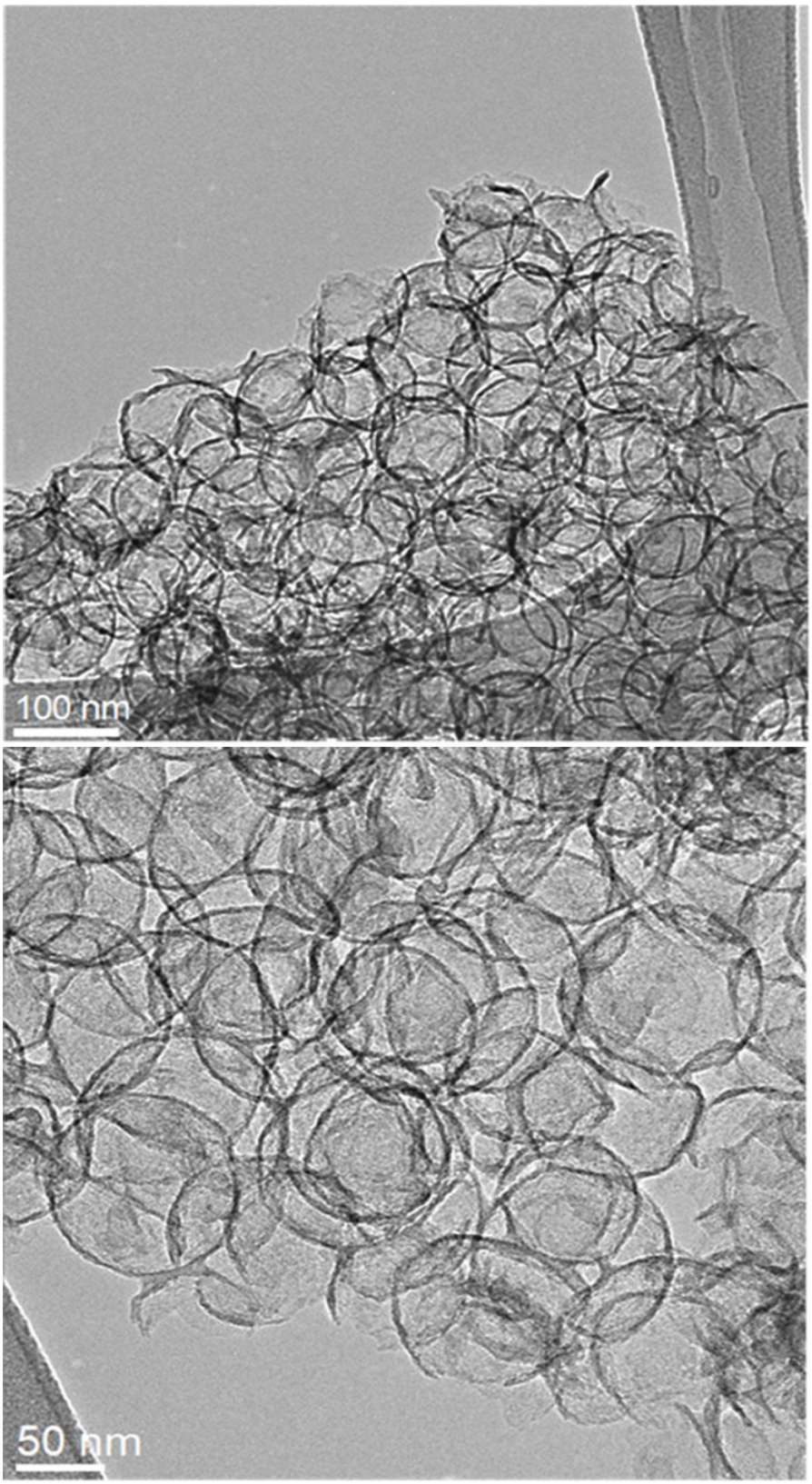

Figure S30 | TEM images of a Q:B HC electrode after 1,000 charging-discharging cycles.

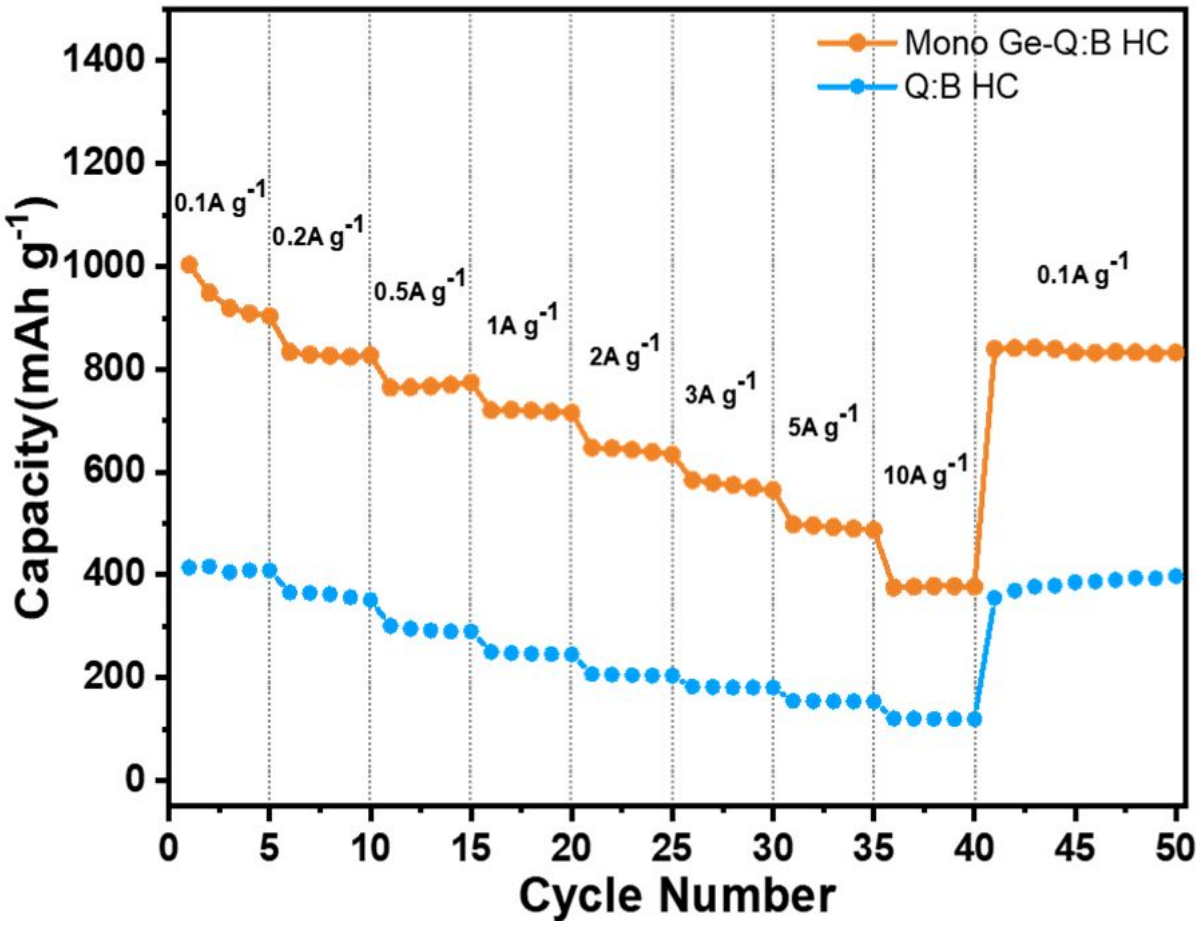

Figure S31 | Specific capacities of Mono Ge-Q:B HC and Q:B HC from the galvanostatic charge/discharge curves.

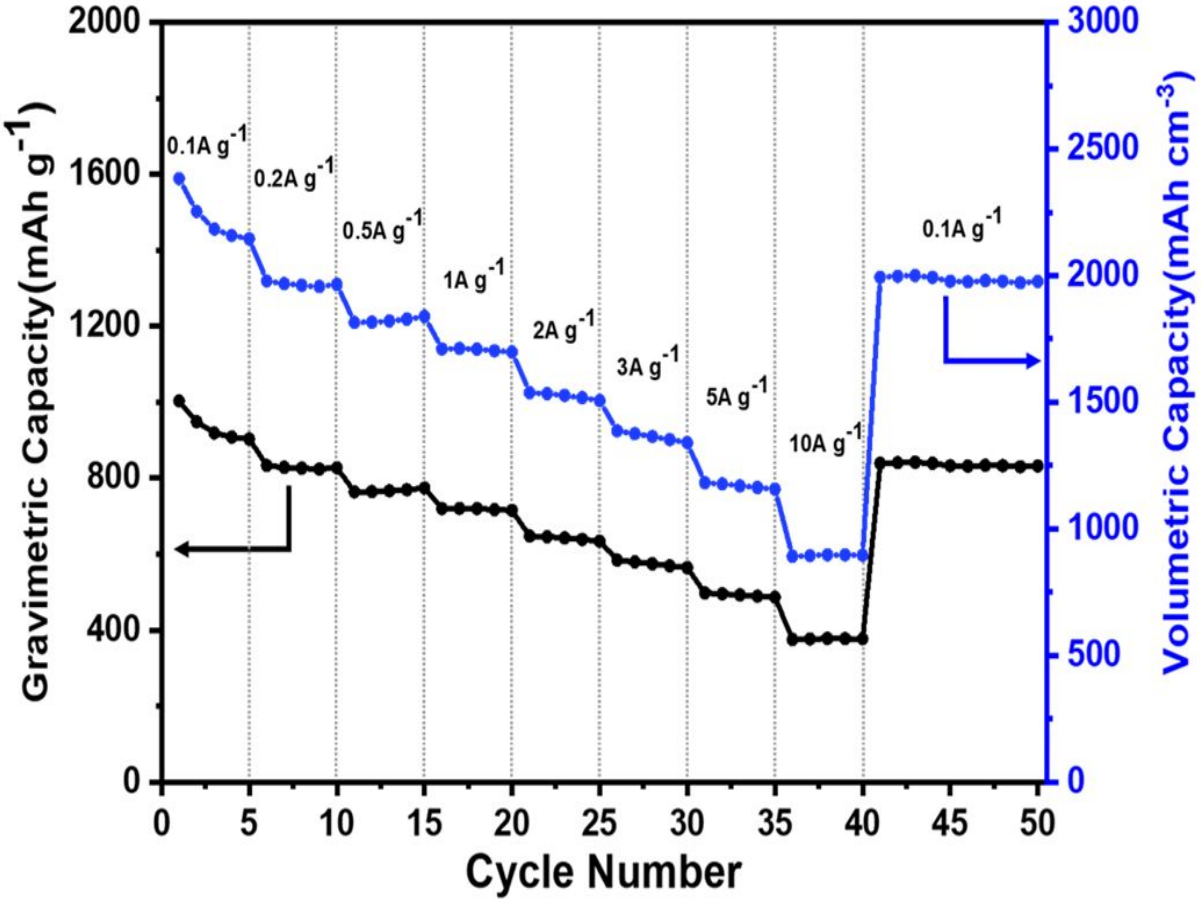

Figure S32 | Comparison of gravimetric capacities and volumetric capacities of Mono Ge-Q:B HC from the galvanostatic charge/discharge curves.

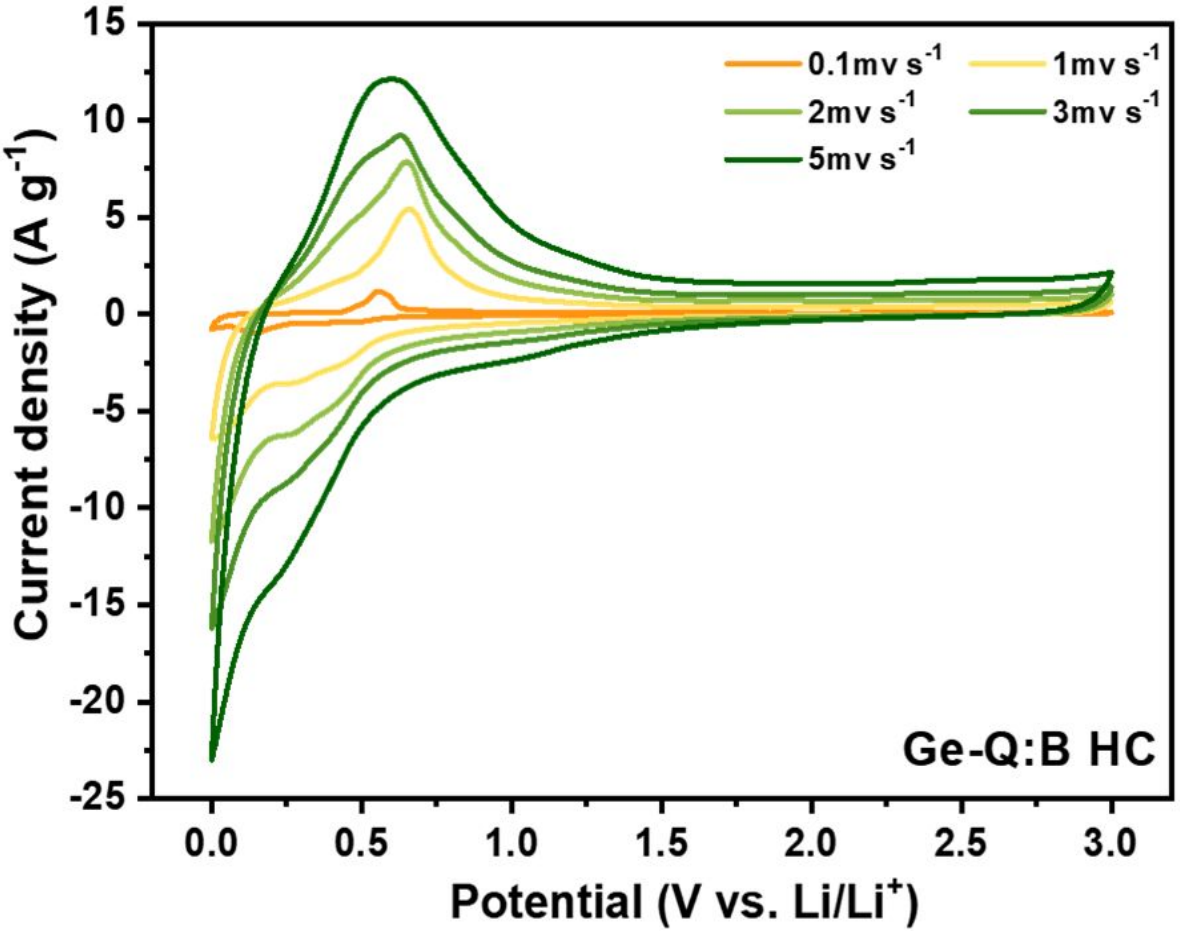

Figure S33 | CV curves of Mono Ge-Q:B HC with the different scan rates from 0.1 mv s^{-1} to 5 mv s^{-1}

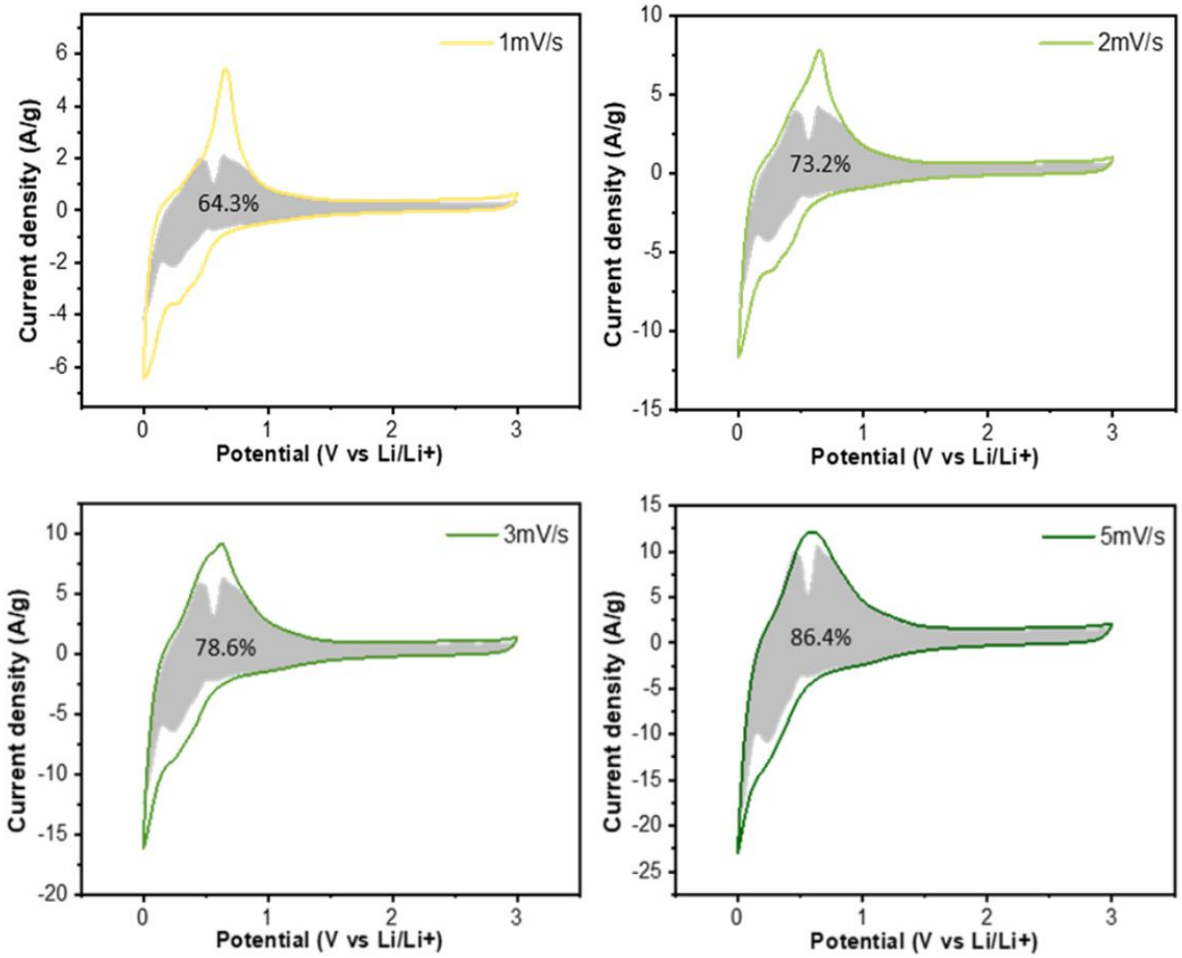

Figure S34 | CV curves of Mono Ge-Q:B HC in the different scan rates, where each capacitive contribution ratio was derived from k_1 and k_2 values.

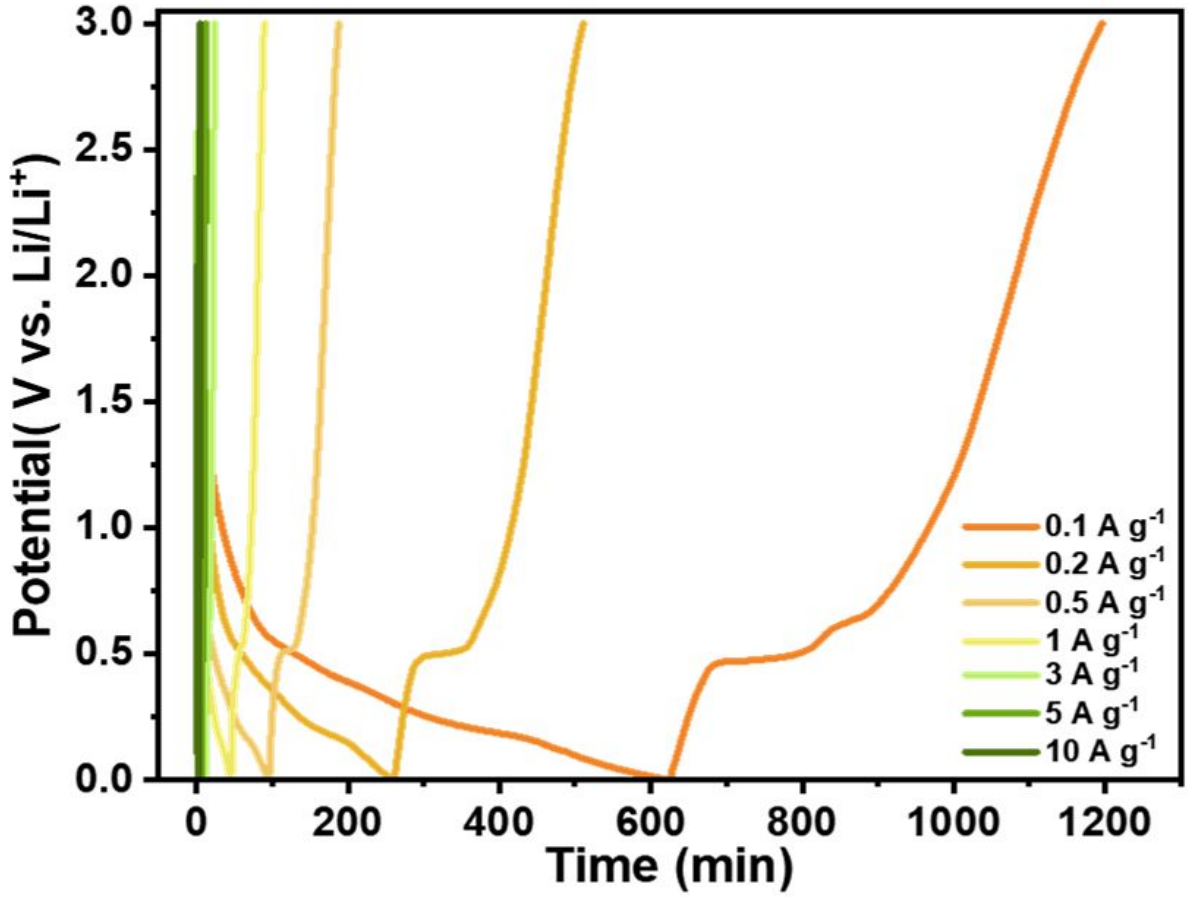

Figure S35 | Galvanostatic charge/discharge (GCD) profiles of Mono Ge-Q:B HC at various current densities.

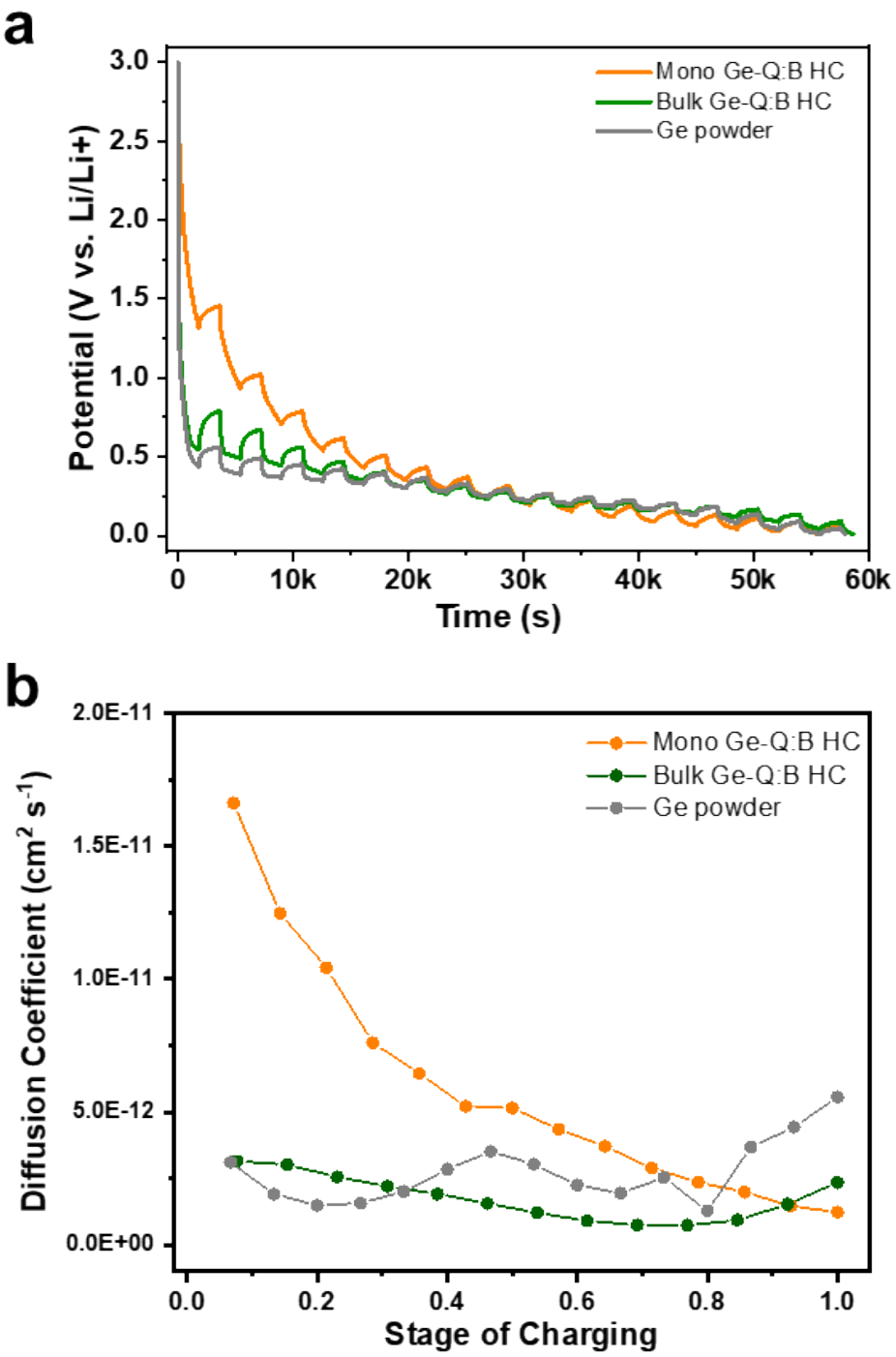

Figure S36 | GITT curves and lithium-ion diffusion coefficients. (**a**) GITT curves of Ge powder, Bulk Ge-Q:B HC, and Mono Ge-Q:B HC after 5 charging/discharging cycles with 30min current pulse and 30 min rest time at 0.1A g^{-1}. (**b**) Lithium-ion diffusion coefficients determined from GITT data.

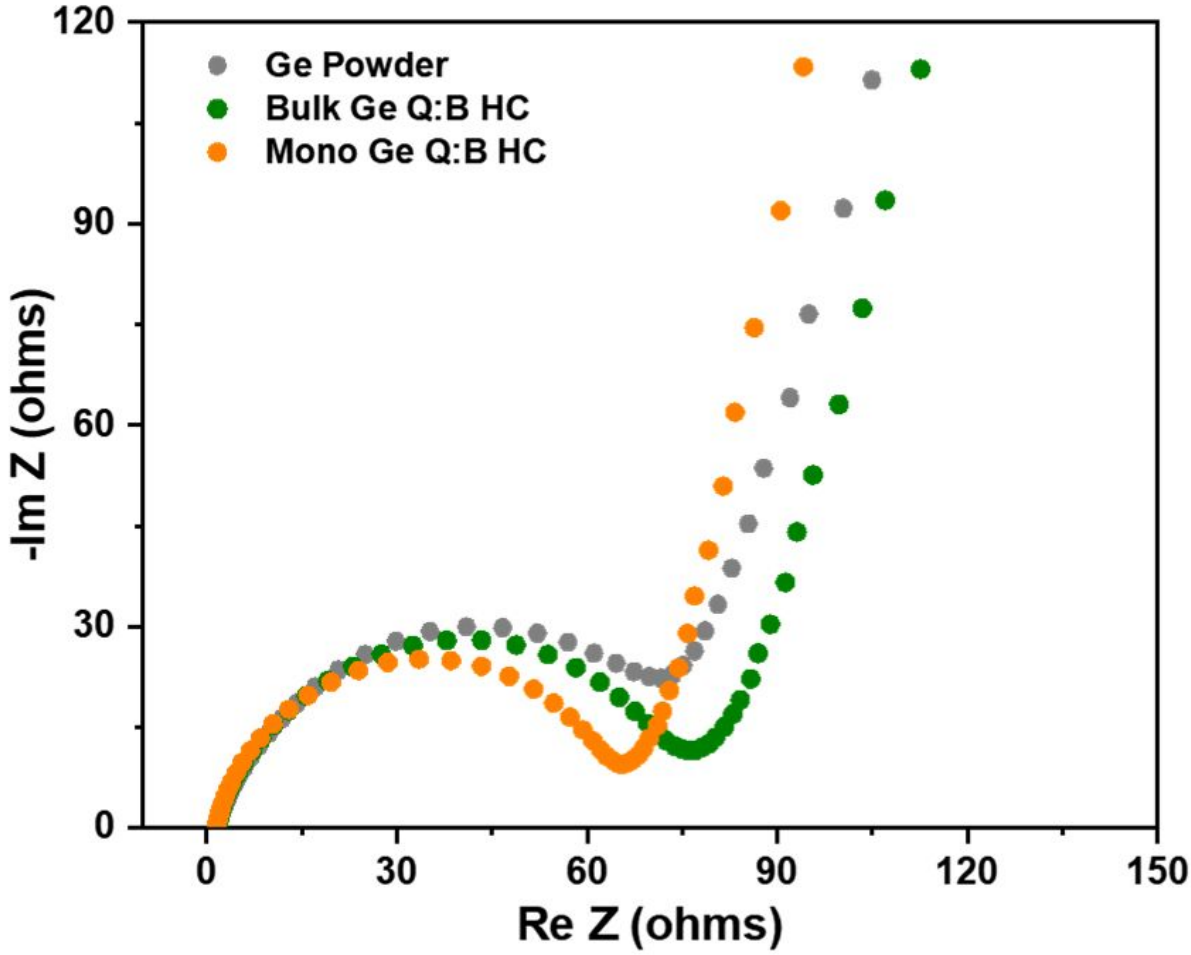

Figure S37 | Nyquist plots of Ge powder, Bulk Ge-Q:B HC, and Mono Ge-Q:B HC in the open circuit voltage(OCV) state condition.

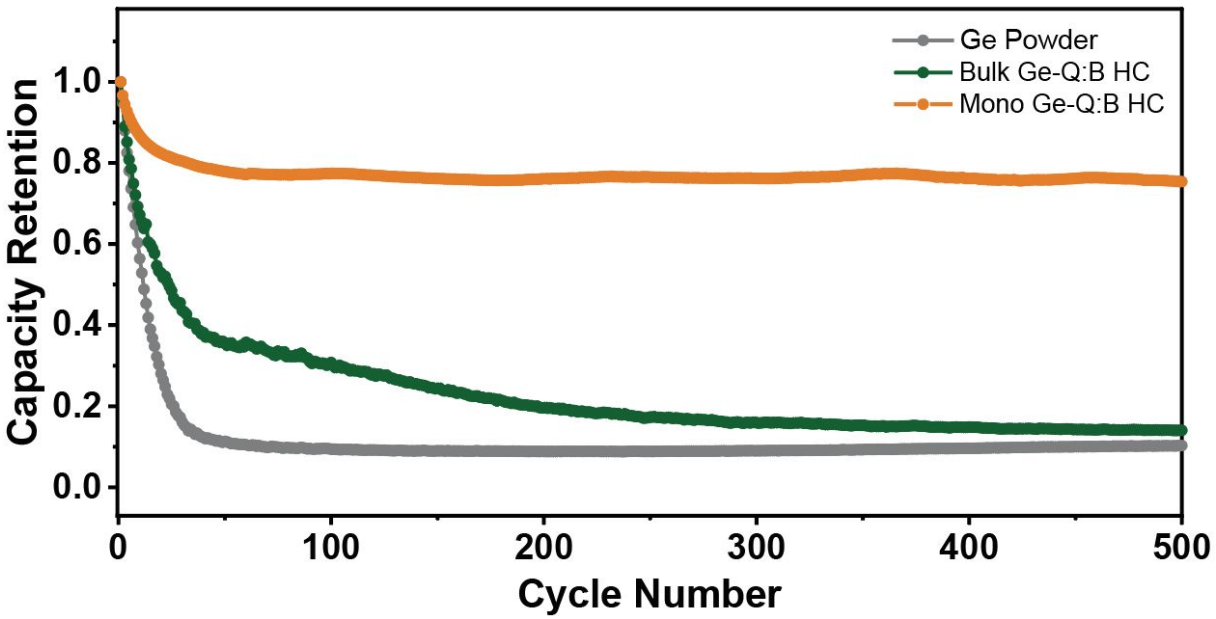

Figure S38 | Cycling performance of the of Mono Ge-Q:B HC, Bulk Ge-Q:B HC and Ge powder at the 2A g^{-1} current density.

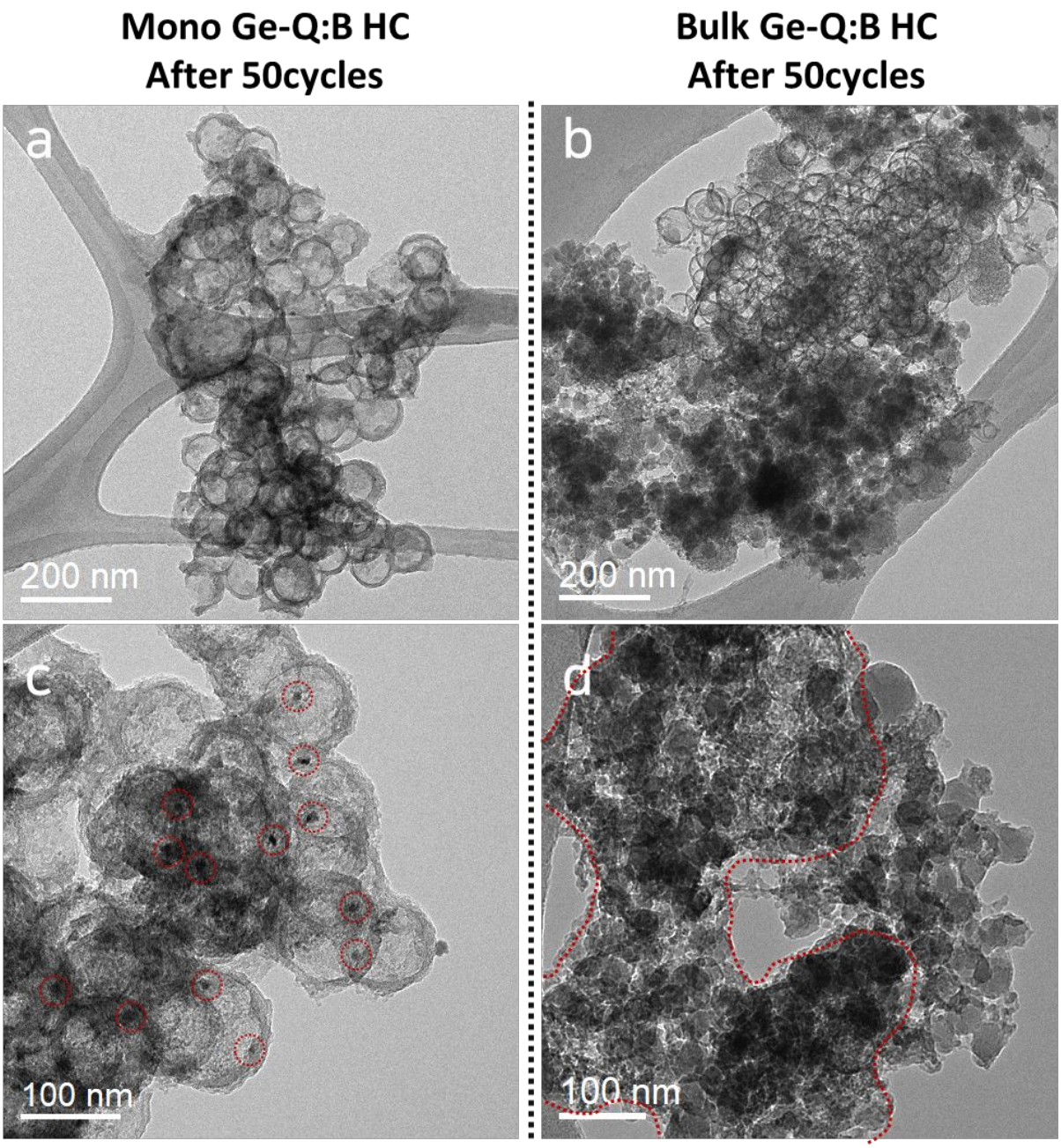

Figure S39 | TEM images of Ge-Q:B HC samples after 50 charging/discharging cycles. Those for Mono Ge-Q:B HC (**a**,**c**) and Bulk Ge-Q:B HC (**b**,**d**).

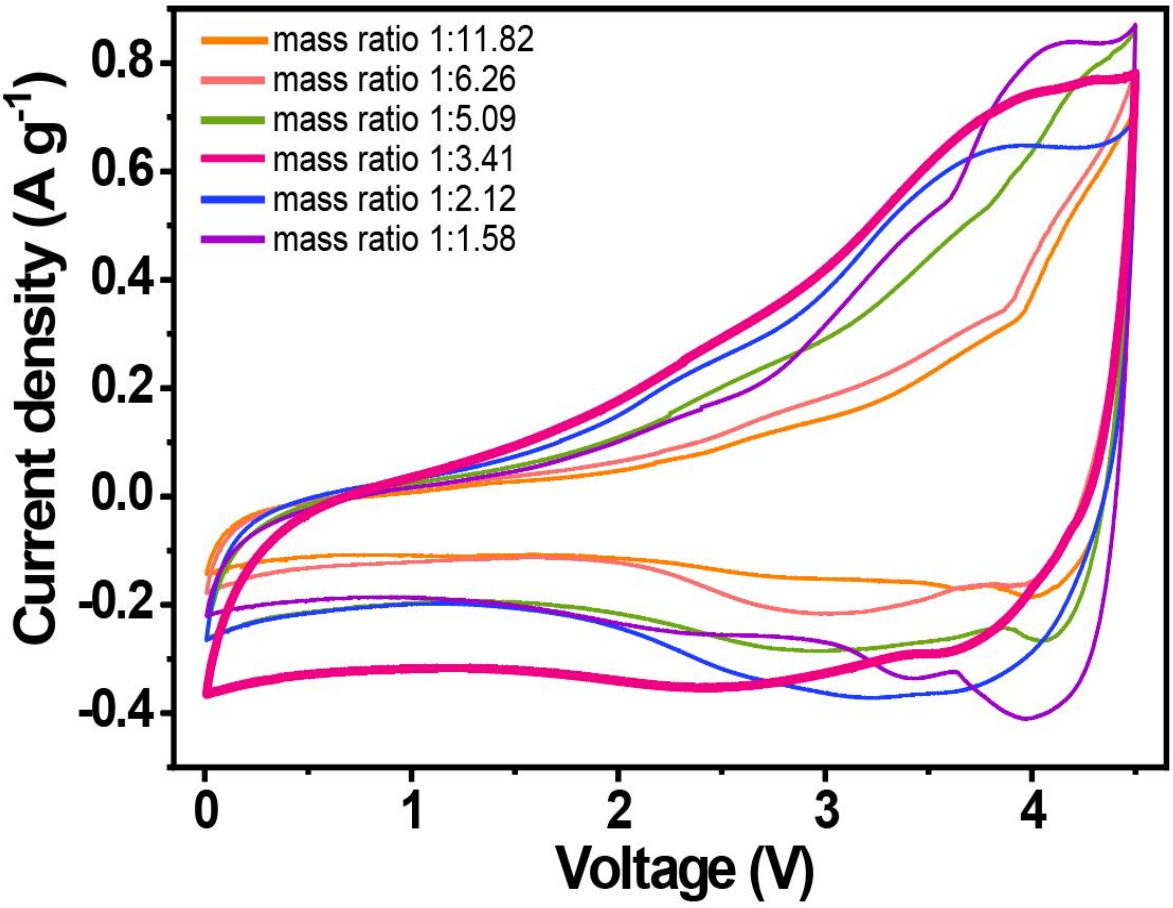

Figure S40 | CV curves of Ge-Q:B HC//Q:B HC full cell with different electrode mass ratio of Ge–Q:B HC to Q:B HC.

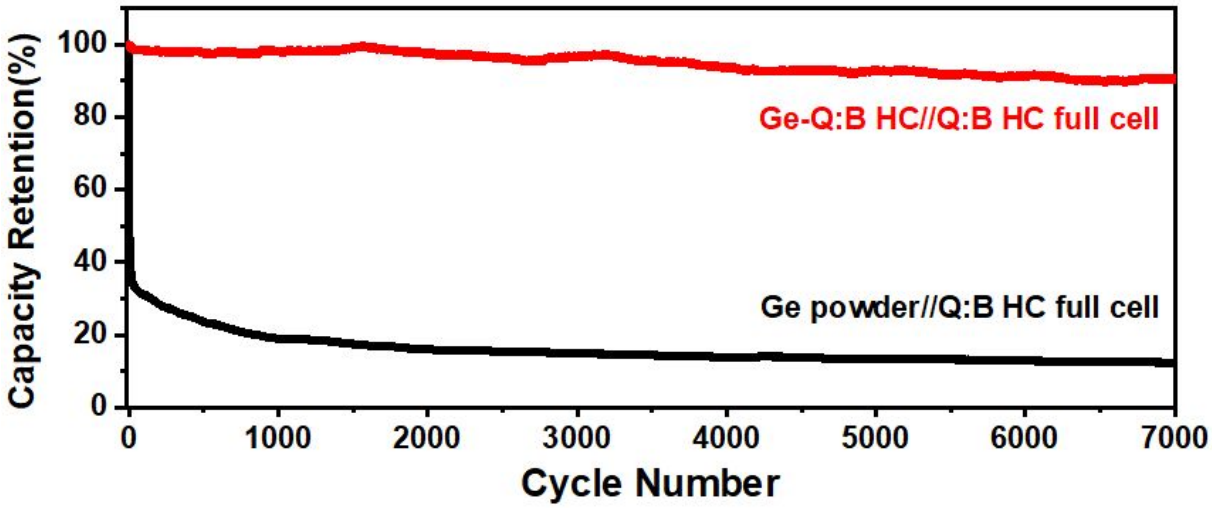

Figure S41 | Capacity retention curves of Ge-Q:B HC//Q:B HC and Ge powder//Q:B HC full cell at 3A g^{-1}.

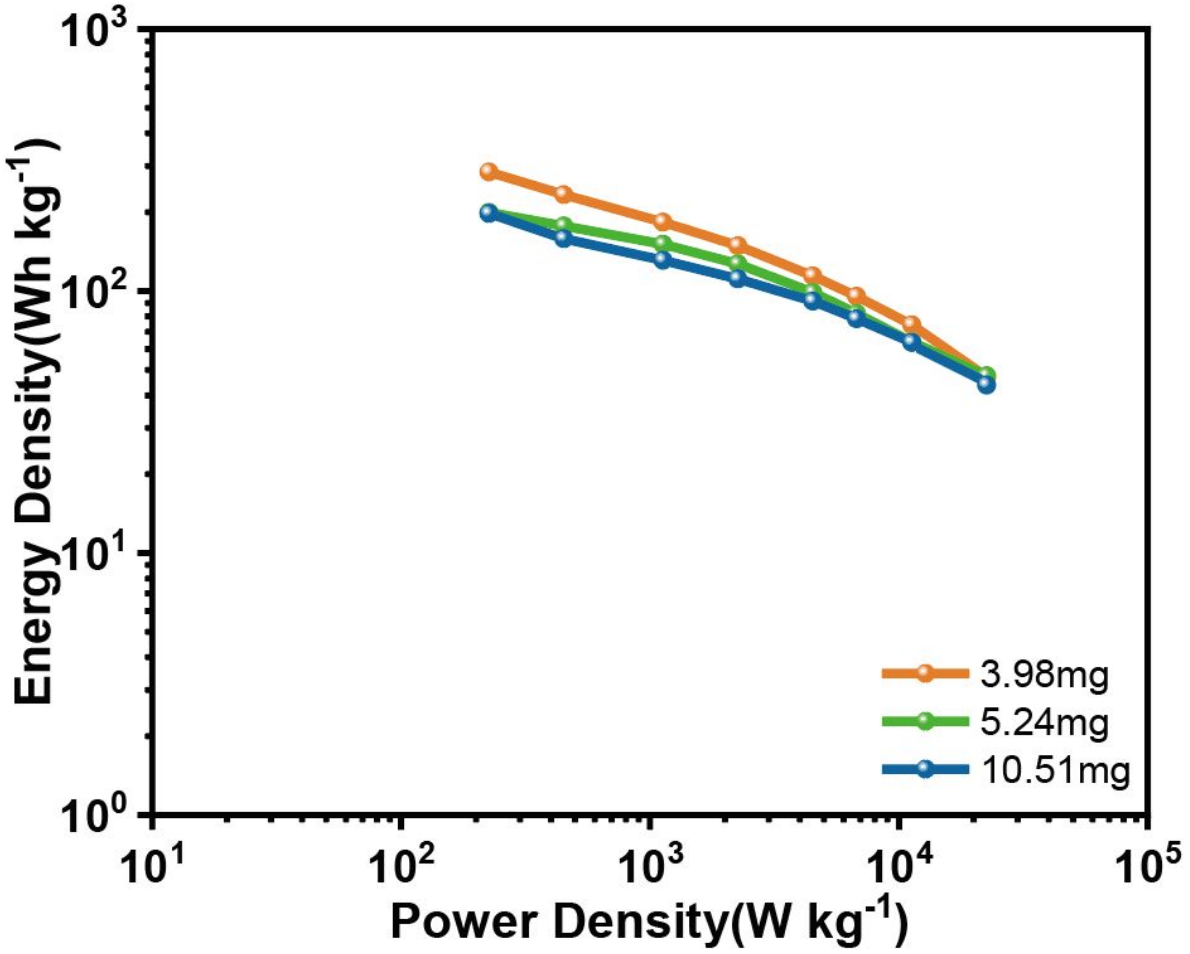

Figure S42 | Ragone plots of Ge-Q:B HC//Q:B HC hybrid energy storage full cells on the different mass loadings.

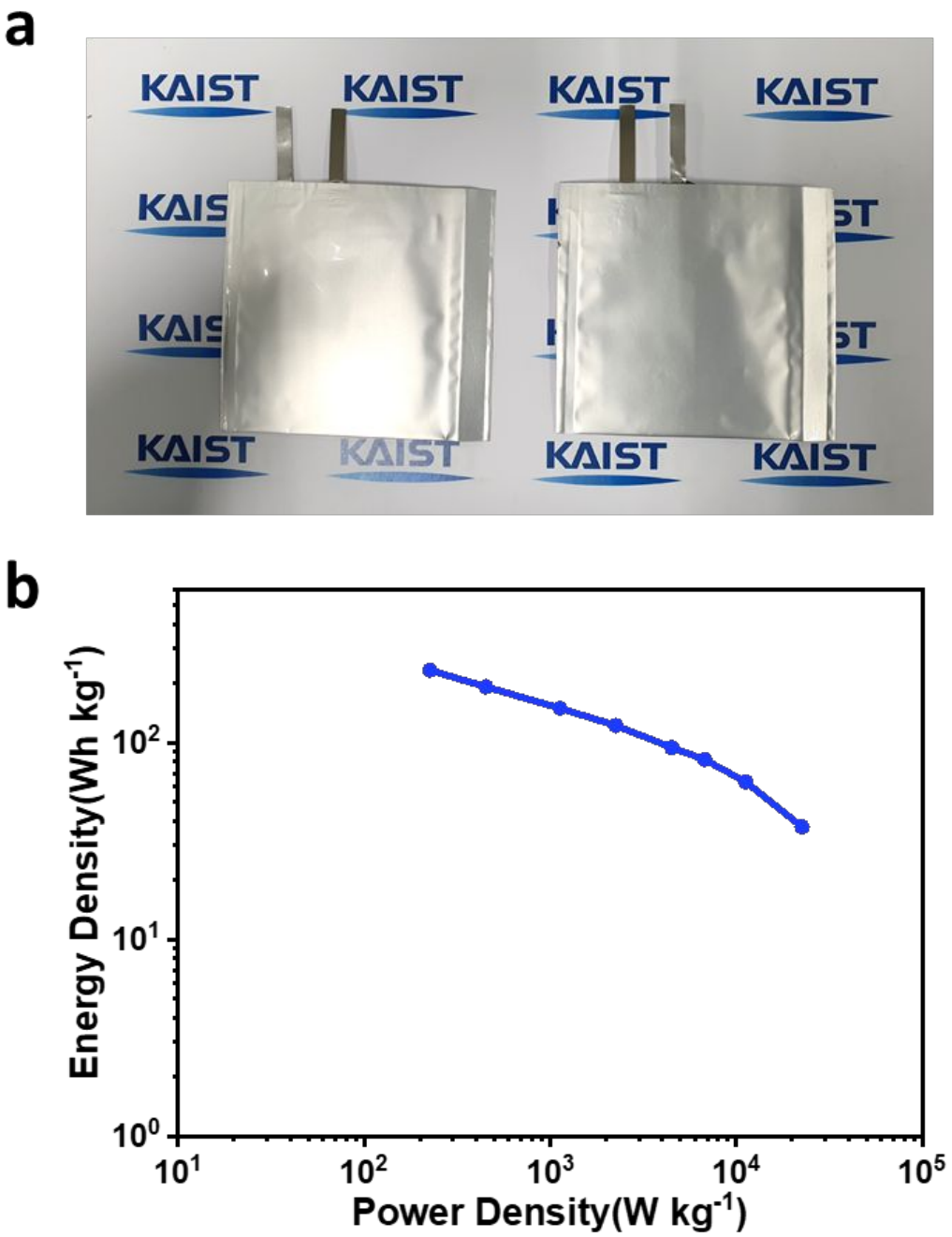

Figure S43 | Ge-Q:B HC//Q:B HC pouch-type full cells. (a) Photos of fabricated Ge-Q:B HC//Q:B HC pouch-type full cells and (b) Ragone plots of Ge-Q:B HC//Q:B HC pouch-type cell.

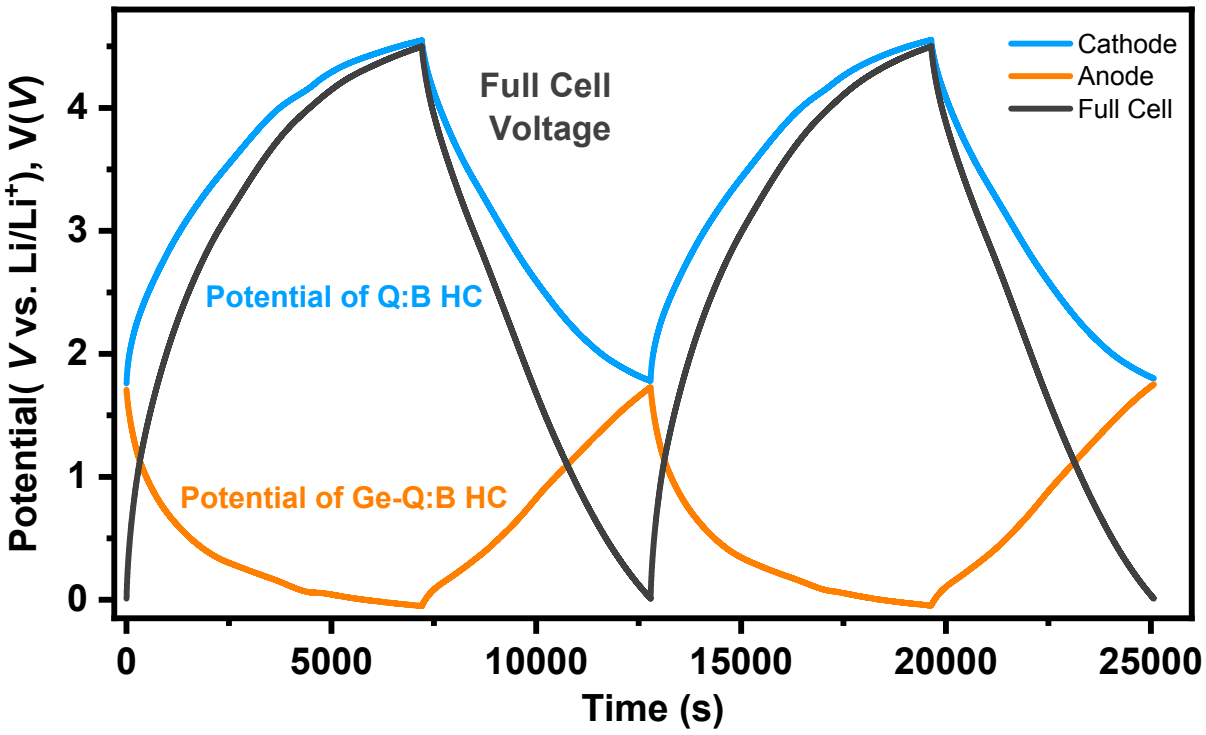

Figure S44 | GCD profiles of the three-electrode full cell (anode: Ge-Q:B HC, cathode: Q:B HC, reference: Li metal foil) as well as the potential range of each electrode.

Table S1 | Electrochemical performances of Ge-Q:B HC//Q:B HC hybrid energy storage full cells at the different current densities.

Energy Density [Wh kg^{-1}]	Power Density [W kg^{-1}]
285	226
233	451
183	1128
149	2255
114	4510
95	6765
74	11275
42	22550

Table S2 | Electrochemical performances of previous works on non-aqueous HES full cells and this work.

Non-Aqueous HES

LIC Full Cells (Anode//Cathode)	Electrolyte	Voltage Range [V]	Max Energy Density [Wh kg^{-1}]	Max Power Density [Wh kg^{-1}]	Ref.
Ge-Q:B HC//Q:B HC	1 M $LiPF_6$ EC/DEC (1:1 vol. %)	0.01-4.5	285 (226 W kg^{-1})	22600 (42 Wh kg^{-1})	This Work
T-Nb_2O_5 nanorod//AC	1 M $LiPF_6$ EC/DEC (1:1 vol. %)	1–3.5	92.1 (80 W kg^{-1})	8000 (35.6 Wh kg^{-1})	(S1)
$LiFePO_4$ embedded rGO&C@$Li_3V_2(PO_4)_3$ // AC	1 M $LiPF_6$ EC/DEC/DMC (1:1:1 vol. %)	1–4	126 (109 W kg^{-1})	3360 (77 Wh kg^{-1})	(S2)
Zr-MOF // AC	1 M $LiPF_6$ EC/DMC (1:1 vol. %)	1–4	122.5 (250 W kg^{-1})	12500 (34.4 Wh kg^{-1})	(S3)
MnO/3DGS//AC	1 M $LiPF_6$ EC/DEC/DMC (1:1:1 vol. %)	1–4	179.3 (139.2 W kg^{-1})	11700 (48.2 Wh kg^{-1})	(S4)
Nb_2O_5 film // AC	1 M $LiPF_6$ EC/DMC (1:1 vol. %)	1–3.5	95.55 (191 W kg^{-1})	5350.9 (65.39 Wh kg^{-1})	(S5)
CNFs-Cu20//AC	1 M $LiPF_6$ EC/DEC (1:1 vol. %)	0.01–4.4	183.2 (220.5 W kg^{-1})	11000 (58.4 Wh kg^{-1})	(S6)
3S-Nb_2O_5-HoMSs//AC	1 M $LiPF_6$ EC/DMC (1:1 vol. %)	1–3.5	93.8 (112.5 W kg^{-1})	22500 (19.6 Wh kg^{-1})	(S7)
$Ti_2Nb_{10}O_{29}$@N-doped Carbon // AC	1 M $LiPF_6$ EC/ DMC (1:1 vol. %)	0.5–4	116.1 (114.6 W kg^{-1})	3171 (63.6 Wh kg^{-1})	(S8)
1T-MoS_2/d-$Ti_3C_2T_x$// GNC	1 M $LiPF_6$ EC/DEC/DMC (1:1:1 vol. %)	0.1–4	188 (168 W kg^{-1})	13000 (22 Wh kg^{-1})	(S9)

Table S3 | Electrochemical performances of previous works on aqueous HES full cells and dual carbon electrode capacitors as well as this work.

Aqueous HES

Electrode Materials (Anode//Cathode)	Electrolyte	Voltage Range [V]	Max Energy Density [Wh kg^{-1}]	Max Power Density [Wh kg^{-1}]	Ref.
$NiMoO_4$ // FeOOH	1M KOH	0-1.5	104.3 (1270W kg^{-1})	10940 (31 Wh kg^{-1})	(S10)
Ni/Co Phosphate 2D nanosheet // AC	3M KOH	0-1.4	33 (600 W kg^{-1})	6000 (26 Wh kg^{-1})	(S11)
NiCoP/NiCo-OH30//Porous C	3M KOH	0-1.6	34 (775 W kg^{-1})	11600 (20 Wh kg^{-1})	(S12)
Ni_xB/G//AC	6M KOH	0-1.65	50 (200 W kg^{-1})	2500 (22 Wh kg^{-1})	(S13]

Dual-Carbon Electrode Capacitors

Electrode Materials (Anode//Cathode)	Electrolyte	Voltage Range [V]	Max Energy Density [Wh kg^{-1}]	Max Power Density [Wh kg^{-1}]	Ref.
GC1100//SFAC	1 M $LiPF_6$ EC/EMC/DMC (1:1:1 vol. %)	2-4	104 (143 W kg^{-1})	6628 (32 Wh kg^{-1})	(S14)
High-defect mesopore-dominant porous carbon// High-defect mesopore-dominant porous carbon	1 M $LiPF_6$ EC/DEC/DMC (1:1:1 vol. %)	1-4	106 (500 W kg^{-1})	8880 (10 Wh kg^{-1})	(S15)
Spiral graphene //Hierarchically porous carbon	1 M $LiPF_6$ EC/EMC/DMC (1:1:1 vol. %)	2-4	109 (1830 W kg^{-1})	5478 (91 Wh kg^{-1})	(S16)
PGCs//AC	1 M $LiPF_6$ EC/DEC/DMC (1:1:1 vol. %)	2-4	83.7 (700 W kg^{-1})	6527 (53 Wh kg^{-1})	(S17)

Section S5. References

(S1) Qin, L.; Liu, Y.; Xu, S.; Wang, S.; Sun, X.; Zhu, S.; Hou, L.; Yuan, C., In-Plane Assembled Single-Crystalline T-Nb_2O_5 Nanorods Derived from Few-Layered Nb_2CT_x MXene Nanosheets for Advanced Li-Ion Capacitors. *Small Methods* **2020,** *4* (12), 2000630.

(S2) Zhang, Y.; Zhang, Z.; Tang, Y.; Jia, D.; Huang, Y.; Pang, W.; Guo, Z.; Zhou, Z., $LiFePO_4$ Particles Embedded in Fast Bifunctional Conductor rGO&C@$Li_3V_2(PO_4)_3$ Nanosheets as Cathodes for High-Performance Li-Ion Hybrid Capacitors. *Adv. Funct. Mater.* **2019,** *29* (17), 1807895.

(S3) Yan, W.; Su, J.; Yang, Z.-M.; Lv, S.; Jin, Z.; Zuo, J.-L., High-Performance Lithium-ion Capacitors Based on Porosity-Regulated Zirconium Metal–Organic Frameworks. *Small* **2021,** *17* (22), 2005209.

(S4) Chen, P.; Zhou, W.; Xiao, Z.; Li, S.; Chen, H.; Wang, Y.; Wang, Z.; Xi, W.; Xia, X.; Xie, S., In situ Anchoring MnO Nanoparticles on Self-Supported 3D Interconnected Graphene Scroll Framework: A Fast Kinetics Boosted Ultrahigh-Rate Anode for Li-Ion Capacitor. *Energy Storage Mater.* **2020,** *33*, 298-308.

(S5) Deng, B.; Lei, T.; Zhu, W.; Xiao, L.; Liu, J., In-Plane Assembled Orthorhombic Nb_2O_5 Nanorod Films with High-Rate Li^+ Intercalation for High-Performance Flexible Li-Ion Capacitors. *Adv. Funct. Mater.* **2018,** *28* (1), 1704330.

(S6) Xue, Y.; Li, Y.; Luo, G.; Shi, K.; Liu, E.; Zhou, J., Using a Dynamic Inhibition Concept to Achieve Content-Controllable Synthesis of N-Coordinated Cu Atoms as Reversible Active Site toward Super Li-Ion Capacitors. *Adv. Energy Mater.* **2020,** *10* (41), 2002644.

(S7) Bi, R.; Xu, N.; Ren, H.; Yang, N.; Sun, Y.; Cao, A.; Yu, R.; Wang, D., A Hollow Multi-Shelled Structure for Charge Transport and Active Sites in Lithium-Ion Capacitors. *Angew. Chem. Int. Ed.* **2020,** *59* (12), 4865-4868.

(S8) Yuan, T.; Luo, S.; Soule, L.; Wang, J.-H.; Wang, Y.; Sun, D.; Zhao, B.; Li, W.; Yang, J.; Zheng, S.; Liu, M., A Hierarchical $Ti_2Nb_{10}O_{29}$ Composite Electrode for High-Power Lithium-Ion Batteries and Capacitors. *Mater. Today* **2021,** *45*, 8-19.

(S9) Wang, L.; Zhang, X.; Xu, Y.; Li, C.; Liu, W.; Yi, S.; Wang, K.; Sun, X.; Wu, Z.-S.; Ma, Y., Tetrabutylammonium-Intercalated 1T-MoS_2 Nanosheets with Expanded Interlayer Spacing Vertically Coupled on 2D Delaminated MXene for High-Performance Lithium-Ion Capacitors. *Adv. Funct. Mater.* **2021,** *31* (36), 2104286.

(S10) Owusu, K. A.; Qu, L.; Li, J.; Wang, Z.; Zhao, K.; Yang, C.; Hercule, K. M.; Lin, C.; Shi, C.; Wei, Q.; Zhou, L.; Mai, L., Low-Crystalline Iron Oxide Hydroxide Nanoparticle Anode for High-Performance Supercapacitors. *Nat. Commun.* **2017,** *8* (1), 14264.

(S11) Li, B.; Gu, P.; Feng, Y.; Zhang, G.; Huang, K.; Xue, H.; Pang, H., Ultrathin Nickel–Cobalt Phosphate 2D Nanosheets for Electrochemical Energy Storage under Aqueous/Solid-State Electrolyte. *Adv. Funct. Mater.* **2017,** *27* (12), 1605784.

(S12) Li, X.; Wu, H.; Elshahawy, A. M.; Wang, L.; Pennycook, S. J.; Guan, C.; Wang, J., Cactus-Like NiCoP/NiCo-OH 3D Architecture with Tunable Composition for High-Performance Electrochemical Capacitors. *Adv. Funct. Mater.* **2018,** *28* (20), 1800036.

(S13) Chen, Y.; Zhou, T.; Li, L.; Pang, W. K.; He, X.; Liu, Y.-N.; Guo, Z., Interfacial Engineering of Nickel Boride/Metaborate and Its Effect on High Energy Density Asymmetric Supercapacitors. *ACS Nano* **2019,** *13* (8), 9376-9385.

(S14) Yang, Z.; Guo, H.; Li, X.; Wang, Z.; Wang, J.; Wang, Y.; Yan, Z.; Zhang, D., Graphitic Carbon Balanced Between High Plateau Capacity and High Rate Capability for Lithium Ion Capacitors. *J. Mater. Chem. A* **2017,** *5* (29), 15302-15309.

(S15) Niu, J.; Shao, R.; Liu, M.; Liang, J.; Zhang, Z.; Dou, M.; Huang, Y.; Wang, F., Porous Carbon Electrodes with Battery-Capacitive Storage Features for High Performance Li-ion Capacitors. *Energy Storage Mater.* **2018,** *12*, 145-152.

(S16) Li, G.; Yin, Z.; Guo, H.; Wang, Z.; Yan, G.; Yang, Z.; Liu, Y.; Ji, X.; Wang, J., Metalorganic Quantum Dots and Their Graphene-Like Derivative Porous Graphitic Carbon for Advanced Lithium-Ion Hybrid Supercapacitor. *Adv. Energy Mater.* **2019,** *9* (2), 1802878.

(S17) Wang, J.; Yan, Z.; Yan, G.; Guo, H.; Li, X.; Wang, Z.; Wang, X.; Yang, Z., Spiral Graphene Coupling Hierarchically Porous Carbon Advances Dual-Carbon Lithium Ion Capacitor. *Energy Storage Mater.* **2021,** *38*, 528-534.